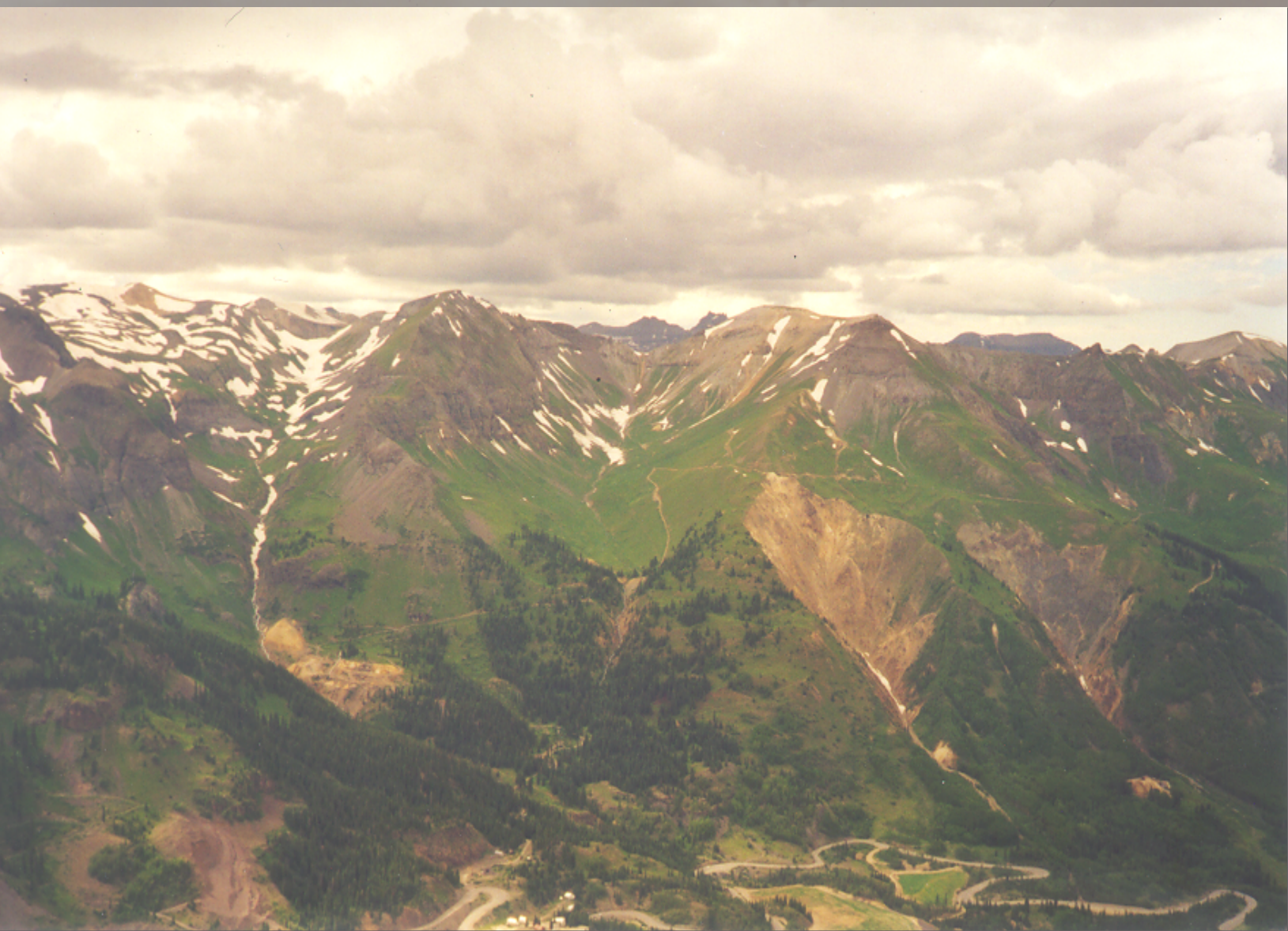# USGS
science for a changing world

Remote Sensing Characterization of the Animas River Watershed, Southwestern Colorado, by AVIRIS Imaging Spectroscopy

Scientific Investigations Report 2004-5203

U.S. Department of the Interior
U.S. Geological Survey

Remote Sensing Characterization of the Animas River Watershed, Southwestern Colorado, by AVIRIS Imaging Spectroscopy

By J.B. Dalton, D.J. Bove, and C.S. Mladinich

Scientific Investigations Report 2004-5203

U.S. Department of the Interior
Gale A. Norton, Secretary

U.S. Geological Survey
P. Patrick Leahy, Acting Director

U.S. Geological Survey, Reston, Virginia: **2005**

Contents

Figures

Remote Sensing Characterization of the Animas River Watershed, Southwestern Colorado, by AVIRIS Imaging Spectroscopy

By J.B. Dalton, D.J. Bove, and C.S. Mladinich

Abstract

Visible-wavelength and near-infrared image cubes of the Animas River watershed in southwestern Colorado have been acquired by the Jet Propulsion Laboratory's Airborne Visible and InfraRed Imaging Spectrometer (AVIRIS) instrument and processed using the U.S. Geological Survey Tetracorder v3.6a2 implementation. The Tetracorder expert system utilizes a spectral reference library containing more than 400 laboratory and field spectra of end-member minerals, mineral mixtures, vegetation, manmade materials, atmospheric gases, and additional substances to generate maps of mineralogy, vegetation, snow, and other material distributions. Major iron-bearing, clay, mica, carbonate, sulfate, and other minerals were identified, among which are several minerals associated with acid rock drainage, including pyrite, jarosite, alunite, and goethite. Distributions of minerals such as calcite and chlorite indicate a relationship between acid-neutralizing assemblages and stream geochemistry within the watershed. Images denoting material distributions throughout the watershed have been orthorectified against digital terrain models to produce georeferenced image files suitable for inclusion in Geographic Information System databases. Results of this study are of use to land managers, stakeholders, and researchers interested in understanding a number of characteristics of the Animas River watershed.

Introduction

The northern part of the Animas River watershed, southwestern Colorado, is the site of a coordinated effort by several Federal, State, and local agencies to characterize the extent and severity of environmental effects from acid mine drainage. This water originates both from numerous historical mine sites that date back as much as a century or more, and from extensive areas of unmined mineralized and hydrothermally altered rocks. The headwaters of the upper Animas River, Cement Creek, and Mineral Creek are associated with the Tertiary San Juan and Silverton volcanic calderas, which were cut by large faults and intense

ring fractures suitable for later mineralization. As part of this study by the U.S. Geological Survey (USGS), the Jet Propulsion Laboratory (JPL) was contracted to acquire AVIRIS data (region outlined in figs. 1, 2) over the San Juan Mountains and Animas River watershed. Methods of infrared spectral analysis developed at the USGS Denver Spectroscopy Laboratory (Clark and others, 1990, 2003) have been applied to characterize the surface distributions of a number of materials. These AVIRIS mineral maps have been used, in conjunction with field geologic mapping, geochemistry, and geophysics, to determine the relative extent of natural and anthropogenic sources of acidic and metal-bearing surface runoff, and their effect on water quality.

The area covered by the data acquisition is bounded approximately by long 108°00' to 107°30' W. and lat 37°15' to 38°00' N. (figs. 1, 2), mainly in Ouray, San Juan, and La Plata Counties, Colo. Also see section, "Watershed Coverage and Study Area."

As part of a larger effort, the purpose of this report is to describe the acquisition, calibration, processing, results, interpretation, and relevance of the imaging spectroscopy data analysis. The processed images detailing surface mineralogy, snow, vegetation cover, and areas of acid-generating and acid-neutralizing potential are included with this report as digital image files. These files are intended to be used by land managers, stakeholders, and scientists, and so have been generated in standard formats. Familiarity with the technology, processing, and interpretation of these images will enable the reader to utilize them most effectively.

The raw imaging spectroscopy data were acquired as image cubes by the high-altitude AVIRIS instrument operated by JPL. Each pixel in an image cube contains a spectrum rather than a single intensity measurement. AVIRIS image cubes cover a visible and near-infrared wavelength range of 0.35 to 2.5 µm (micrometers). The cubes were converted to reflectance using standard atmospheric correction and ground calibration techniques (Gao and others, 1997; Clark and others, 2002). The calibrated cubes were then processed using the USGS Denver Tetracorder 3.6a2 algorithm to create

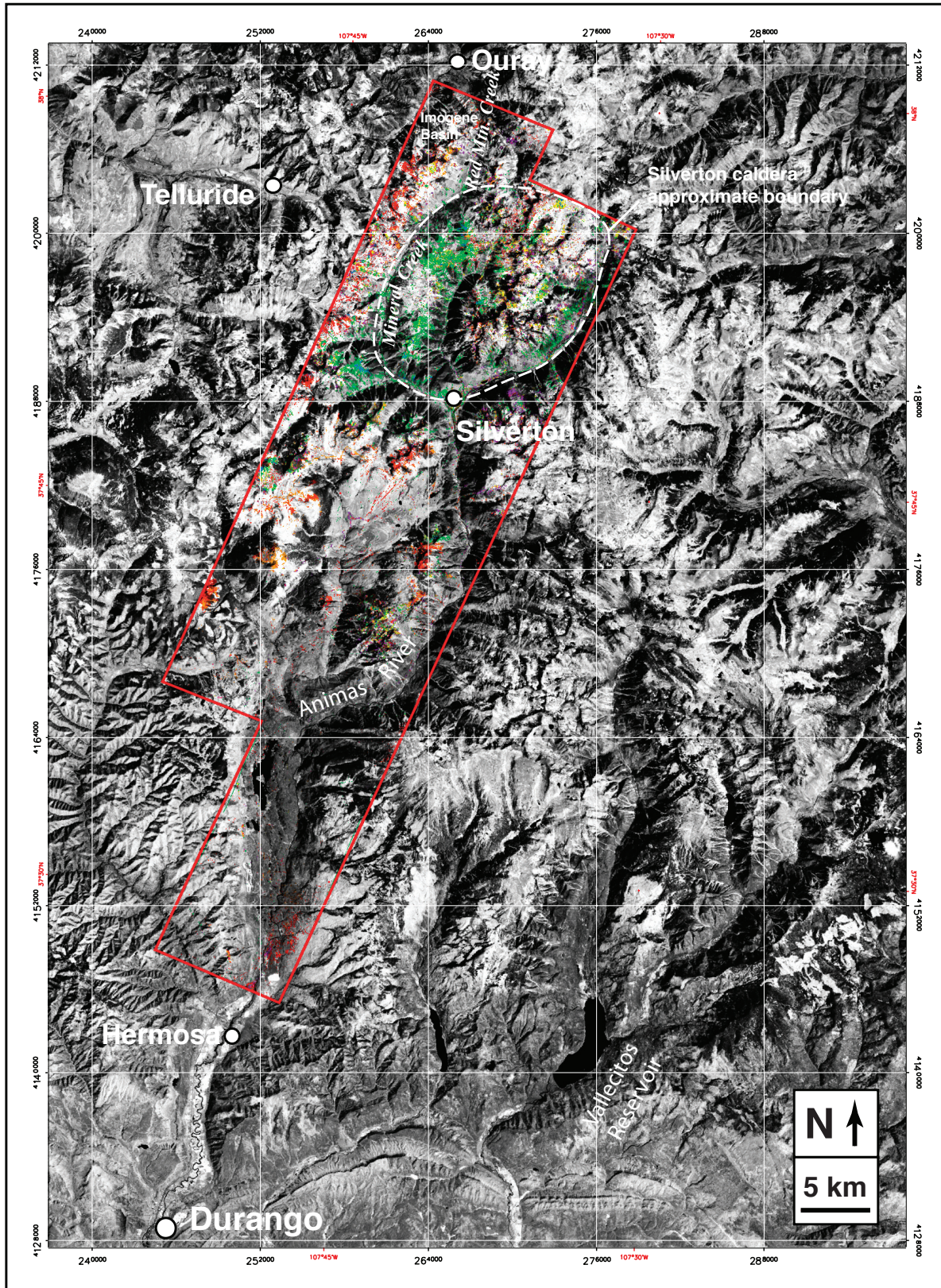**Figure 1.**   Animas River AVIRIS flightlines (red outline) overlaid upon Landsat Thematic Mapper (TM) band 4 imagery. Major geographic features are shown. Animas River flows along right-hand edge of AVIRIS study area. Silverton caldera is roughly bounded by upper Animas River, Mineral Creek, and Red Mountain Creek. Highly mineralized zones of Silverton caldera dominate northeastern section, including upper Animas River headwaters.

preliminary two-dimensional image maps detailing surface distributions of materials on the basis of comparison with reference spectra from the USGS Digital Spectral Library (Clark, Swayze, Gallagher, and others, 1993). The preliminary image maps were then evaluated and field-checked. Rock and mineral samples acquired during field studies were analyzed and added to the spectral library, and the Tetracorder process was repeated to refine the image maps. Once the results were found to be satisfactory, the final image maps were compiled into color-coded overlay images for minerals and other materials of interest (such as snow and vegetation). These color images were then corrected for motion of the AVIRIS sensor, mosaicked together, registered to a map base, and orthorectified using a digital terrain model. The orthorectified images are included with this report, and a considerably reduced subset of the image set is included in the figures.

Acknowledgments

Image Format Considerations and Associated Files

The large size (>1,200 km^2) and small-scale complexity (< 1 m) of the study area leads to image manipulation considerations which make publication and navigation of the imaging spectroscopy results in a traditional format unwieldy. In order to present as complete an analysis as possible, the images are made available in multiple formats. The most effective way to utilize the following sections is to access the georeferenced images via any image manipulation software that allows zoom and pan functions. The reader may then view all of the image detail while reading the text and referring to topographic maps. There is far too much detail to present all of the map contents within the report; rather, examples have been prepared that highlight the types of issues addressed in the watershed study and illustrate reasonable approaches to interpretation of the mineral maps. The georeferenced images can be compared to a map base using a GIS program, or overlaid on the USGS 7.5-minute topographic map series by printing them out at 1:24,000 scale on a large-format printer. Each pixel is 17.5 m (meters) on a side, and each flightline is 614 pixels wide. Whereas the entire study area lies within the Durango 1:250,000-scale map, this scale is too compact to view many of the details in the AVIRIS data. The following 7.5-minute maps will be most useful: Ouray, Ironton, Handies Peak, Ophir, Silverton, Howardsville, Engineer Mountain, Snowdon Peak, Electra Lake, and Hermosa (U.S. Geological Survey, Denver). Additional neighboring maps may be desired to completely cover the margins of the study area but are not essential to utilize the information presented in this report.

Image Color Tables and Printing Concerns

The colors used for particular material classes in the images were arrived at through several years experience working with AVIRIS data in many locations. They represent a balance between several criteria, including the capabilities of display monitors, the need to discriminate adjacent pixels by eye, the limitations of human vision, aesthetic concerns, and the desire to include as many materials as possible in a scene. It was also important that related minerals be represented by related colors—or, in some cases, by highly contrasting colors. The most demanding requirement was the fact that color printers in general are not capable of perfectly duplicating the colors seen on a display monitor. The colors used for this study produce the closest attainable correspondence between display colors and ink colors. At the time of publication, not all commercially available color printers faithfully reproduce the colors and details required for utilization of these images; some printers may produce images with too little contrast or color discrimination. The reader is advised to print the color keys provided and examine them before printing the full-scale images. The page-size mineral maps presented here are also compromised in that they have been reduced to half-size to fit on the page. The resolution of these images is such that adjacent pixels must be averaged together to print them in an 8.5×11 inch format, and so the printed figures will of a necessity be less clear than the digital versions. If a suitable printer cannot be located, it is advisable to deal directly with the digital images. Many image manipulation software programs allow the user to modify image color tables to suit various needs; this is recommended only as a last resort and should be conducted with caution.

Image Format Considerations

Several image formats were utilized in the analysis leading to this report. Translating AVIRIS infrared image cubes into ordinary images proceeds via several steps, each with its own attendant complications. Because of the number of materials being considered and the need for many colors to display

them, each location must be presented as several images. A further complication arises from the fact that the AVIRIS flightlines were not acquired in a strictly north-south orientation (fig. 1). As a result, the georeferenced image mosaics contain a great deal of blank space. In order to accommodate all the data in a usable format, the discussion that follows will be accompanied by images displaying highlights of the study region. The locations of these images are shown in figures 1 and 2.

The classification images are categorized according to breakdowns detailed in the section on Tetracorder results: Iron Oxide Family (Group 1) minerals, Alteration Products (Group 2), Snow and Vegetation (Group 3), Minerals Associated with Acid Generation (Group 4), and Minerals Associated with Acid-Neutralizing Potential (Group 5, Calcite-Chlorite-Epidote-Sericite). Each group is presented on a black background for improved visibility; the georeferenced images can be imported to a GIS database and manipulated accordingly. For field use, navigation, and comparison to map bases and other image products, however, it is often more useful to have the color-coded material results overlaid on a grayscale image of the scene. This shows roads, water bodies, and other useful landmarks in a format that is more intuitive than the pure classification results. Georeferenced grayscale images are included with the pure classification results. However, within the text, only the grayscale images will be used. This is more than sufficient to follow the discussion, and results in a readable paper which is still useful and informative without recourse to an image display device.

Brief Geologic History of the Study Area

The majority of the report focuses on the geology of areas A, B, and C (fig. 2), principally the drainage areas of the upper Animas River, Cement Creek, and Mineral Creek. This area lies in the western part of the mid- to late-Tertiary age San Juan volcanic field (Lipman and others, 1976; Bove and others, 2000). The geology of areas D and E (fig. 2) is different; only brief geologic comments are included herein, in the section, "Imaging Spectroscopy Tour of Study Area," including comparisons with the more strongly mineralized areas. The local geology is largely lavas and related volcanic rocks associated with the San Juan caldera and the younger Silverton caldera (Steven and Lipman, 1976). Collapse of these calderas created ring fractures that provided conduits for later episodes of intense hydrothermal alteration and mineralization commonly associated with dacitic to rhyolitic intrusions (Casadevall and Ohmoto, 1977; Lipman and others, 1976). More recent geologic activity has been dominated by uplifts during the Neogene (Steven and others, 1995), followed by downcutting and the formation of the upper Animas River and its tributaries, with brief episodes of sediment deposition.

Gold was discovered in the San Juan Mountains in 1871, and within the next two decades, upwards of a thousand mining claims were staked in the upper Animas River and Animas River tributaries upstream of the town of Silverton. The Denver and Rio Grande Railroad was extended from Durango to Silverton in 1882; ore production continued at various levels until 1991, when the Sunnyside mine directly upstream from Silverton was closed (Bird, 1999). Remediation of private holdings in the region is ongoing, and this project is partly concerned with evaluating remediation needs of the area, including the thousands of historical prospects and mines on both Federal and private properties.

Mineralization and Hydrothermal Alteration

The collapse of the San Juan caldera, the associated Uncompahgre caldera, and the Silverton caldera at 28–27 Ma provided a favorable structural environment for later mineralization and hydrothermal activity that postdates these calderas by about 5–15 million years (Lipman and others, 1976; Bove and others, 2001). In general, hydrothermal activity temporally associated with caldera development caused regional propylitization characterized by the presence of chlorite, epidote, calcite, and illite, along with incipiently altered primary feldspars. This alteration assemblage, which characterizes a large portion (fig. 2, A, B, C) of the study area of this report, is generally only very weakly pyritic and is important for its acid-neutralizing potential (Bove and others, 2000). Most mineralization and associated hydrothermal alteration in this area are temporally and genetically associated with three major episodes of high-level magmatism between about 27 and 10 Ma (Bove and others, 2001).

Mo-Cu Porphyry Alteration and Mineralization (26–25 Ma)

The earliest important mineralizing and related hydrothermal event within the study area occurred about 26–25 Ma and was related to a large swarm of calc-alkaline intrusions emplaced over a broad region of the western San Juan Mountains (Bove and others, 2001). The only known mineralized hydrothermal system of this type and age within the study area involves peak 3,792 m, situated between the South and Middle Forks Mineral Creek, and its immediate area. However, several large zones of weak sericite-pyrite (WSP) to quartz-sericite-pyrite (QSP) altered rock related to 26 Ma granitic to quartz monzonite intrusions are present in a zone south of the upper Animas River from Cunningham Creek east to Maggie Gulch. An area comprising more than 2 km^2 of intensely altered and pyritized rock is related to a 25 Ma low-grade porphyry Mo-Cu (molybdenum-copper) hydrothermal system. The main zone of Mo-Cu anomalies is coincident with intense QSP-altered rock, high-density quartz-stockwork veining, abundant gypsum, and as much as 5 volume percent
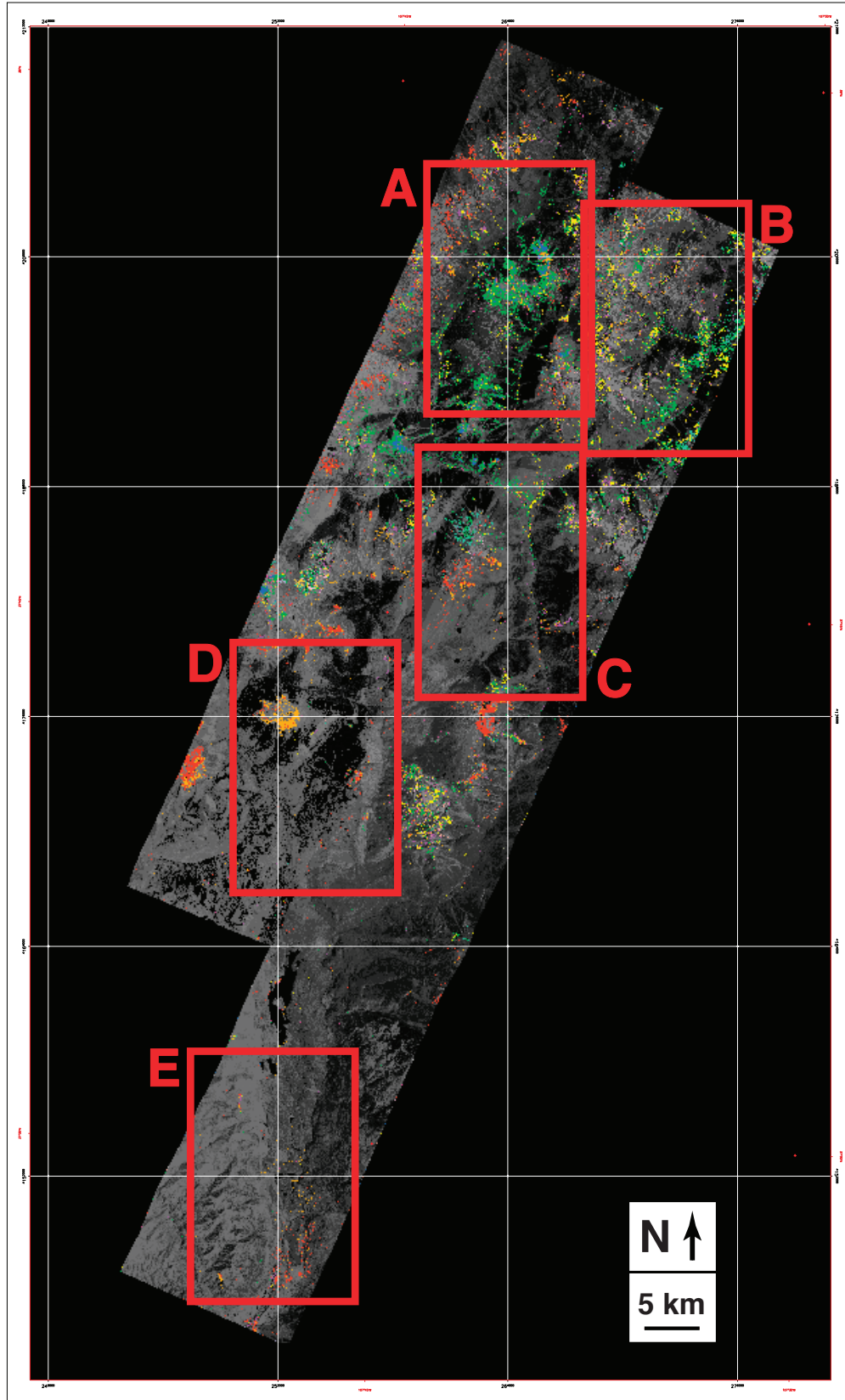
Figure 2.   Overview of AVIRIS imagery for Animas River watershed: A, Ironton and Red Mountain; B, Animas Forks; C, Silverton and Molas Lake; D, Engineer Mountain; E, Hermosa. This is a mosaic of Group 1 materials, overlaid on a grayscale and having the same color scheme and explanation as figure 13.

disseminated sulfides (McCusker, 1982). QSP-altered rock grades outward through weak sericite-pyrite and into propylitized rock (Ringrose and others, 1986; Bove and others, 1998). Unpublished exploration data (McCusker, 1982) indicate that oxidation and supergene leaching is present to depths of as much as 100 m below the mountain tops. Secondary minerals formed within this zone include hematite, goethite, ferrimolybdenite, and minor secondary copper sulfides, including chalcocite, digeonite, and covellite.

Acid-Sulfate Alteration and Mineralization (23 Ma)

The Animas River watershed study area hosts two large acid-sulfate hydrothermal systems. The Red Mountain system, encompassing an area of roughly 20 km², experienced significant and economically important Ag-Cu-Au breccia pipe and fault-hosted mineralization (Bove and others, 2000). The Ohio Peak–Anvil Mountain acid-sulfate system to the south comprises about 18 km² of hydrothermally altered materials; however, this system is mostly devoid of important mineral deposits. Both are located along the structurally complex northwest and southwest margins of the 27 Ma Silverton caldera, between Cement and Mineral Creeks.

Some of the richest ores in the Silverton area were mined from small silicified breccia pipes associated with the extensive acid-sulfate hydrothermal system in the Red Mountains district. These high sulfidation deposits, which mainly formed within the oxidized portions of the breccia pipes, were irregular in shape and typically consisted of carbonates of lead and iron, as well as lead sulfates, iron oxides, sphalerite, and miscellaneous arsenates (Fisher and Leedy, 1973). Below the oxidized zone, sulfide ores of pyrite, enargite and lesser chalcopyrite, galena, tetrahedrite, and sphalerite were present as irregular masses in altered volcanic rocks.

The acid-sulfate mineral assemblages at both localities formed dominantly by the replacement of the original volcanic host by low-pH, magmatic SO_4-rich solutions, as evidenced by the preservation of the original porphyritic rock textures. Excellent outcrop exposure in the Red Mountain and Ohio Peak–Anvil Mountain areas has allowed detailed zonation studies of hydrothermal assemblages within these complex acid-sulfate hydrothermal systems (Bove and others, 2000; Dalton and others, 2000; Mast and others, 2000). Surface mapping and careful paragenetic studies demonstrate that structurally controlled zones of quartz-alunite altered rock transition outward into pyrophyllite, dickite, smectite, and (or) pyrophyllitic assemblages, respectively. Mineralogic data from exploration drilling in the vicinity of Red Mountain #3 and adjacent Prospect Gulch (Bove and others, 2000; Wirt and others, 2001) found that the acid-sulfate alteration zones extend at least 300 m beneath the surface.

Mineralization and Intrusions (<18 Ma)

Economically important post-20 Ma vein mineralization in the western San Juan Mountains appears to have been closely associated with intrusion of high-silica alkali rhyolite (Lipman and others, 1973). The Sunnyside, Gold King, Camp Bird, and Idarado mines were all sited on these polymetallic (Au, Ag, Pb, Zn, Cu) veins, which formed as fracture or fissure fillings that commonly range from less than a meter to tens of meters in width. Veins within the San Juan and inner nested Silverton calderas are either concentric or radial to the ring fracture zone, as in the South Silverton district (Cunningham Creek to Kendall Mountain; Varnes, 1963), or trend parallel to graben-related faults in the resurgent dome of the San Juan–Uncompahgre calderas (Burbank and Luedke, 1969). Hydrothermal alteration related to the veins consists of narrow (1–5 m) envelopes with quartz-sericite-pyrite-kaolinite-calcite-chlorite mineralogy superimposed over regionally propylitic altered rock (Ransome, 1901; Burbank and Luedke, 1969).

High-silica rhyolite intrusions such as those present near Houghton Mountain and California Mountain are petrologically very similar to Climax-type high-silica rhyolites (Lipman and others, 1976; White and others, 1981) that are associated with large molybdenum porphyry systems in the western United States. In some instances these volatile-rich intrusions formed large haloes of intense quartz-sericite-pyrite altered rock and are associated with dense stockwork quartz veinlets.

AVIRIS Data Acquisition and Calibration

The application of remote sensing technology to problems of mine site remediation and acidic drainage has been shown to provide cost-effective solutions to large-scale remediation problems (Swayze, Smith, and Clark, 2000; Swayze, Smith, Clark, Sutley, and others, 2000). Effective utilization of the acquired information is best achieved with some understanding of the method and its limitations. The following section is intended to briefly familiarize the reader with the AVIRIS instrument, its mode of operation, and the methods employed to calibrate the data and present them in a useful form for geophysical studies.

Instrument Description

The AVIRIS instrument (Porter and Enmark, 1987; Green and others, 1988, 1998) utilizes a rotating mirror to sweep the field of view perpendicular to the direction of motion. The foreoptic system focuses light from each pixel in the ground track onto a set of fiber optics, which transmit the light to four spectrometers. Within each spectrometer, light is dispersed via a grating to a linear array of detectors.

Each spectrum thus acquired features 224 channels covering the spectral range from 0.35 to 2.5 µm, with a spectral sampling of 10 nm (nanometers) and 10 nm full-width at half maximum (Green and others, 1998). For this study, the instrument was flown at approximately 20 km altitude aboard the NASA ER-2 airplane, a modified version of the high-altitude U-2 plane.

Watershed Coverage and Study Area

The AVIRIS data were acquired on June 18, 1996, under cloudless skies. Two northeast-southwest-trending, parallel, 10-km wide flightlines with an overlap of approximately 2.5 km were flown (fig. 1). The image is bounded approximately by long 108°00' to 107°30' W. and lat 37°15' to 38°00' N. The first flightline runs from the confluence of Red Mountain Creek and the Uncompahgre River to the Hermosa Cliffs just south and east of the East Fork Hermosa Creek. The second line runs from just upstream of the town of Hermosa, Colo., to the headwaters area of the upper Animas River at Animas Forks, Colo. These two flightlines cover the Animas River itself from its headwaters to just upstream of Hermosa Creek, as well as the entire source area for two major Animas River tributaries, Cement and Mineral Creeks (including South Fork Mineral Creek). These two creeks originate within the caldera and are strongly affected by acidic mine drainage. All but the most distant reaches of the other tributaries in the watershed upstream of Hermosa Creek are part of the AVIRIS data set, including Cunningham, Cascade, Elk, and Lime Creeks. Most of the acidic drainage has been shown to originate within the limits of the overflight (Church and others, 1997). The

towns of Durango and Telluride lie just outside the study area, whereas the town of Silverton is within the second flightline, between the confluences of Cement and Mineral Creeks with the Animas River.

The region outlined in figure 1 is covered by the Durango 1:250,000-scale topographic map (U.S. Geological Survey, 1976) and numerous maps at larger scales. Molas Lake, near Silverton, and the much larger Electra Lake north of Hermosa both lie within the study area. The Vallecito Reservoir in the lower right of the Landsat image is not included in this study, nor are the mostly roadless San Juan National Forest and Weminuche Wilderness to either side of the AVIRIS flightlines. The colors within the AVIRIS overflight area correspond to minerals associated with hydrothermal alteration zones and to iron-bearing precipitates detected downstream from the caldera regions.

Geometric Considerations

Interference from spectral absorptions and scattering in the atmosphere, inherent motion of the sensor platform, and the orientation and topography of the study region all affect the interpretation of AVIRIS data. The rugged San Juan Mountains present some of the most extreme topographic relief encountered in AVIRIS studies so far, with elevation changes exceeding 1.8 km in some places. Because the intensity of light decreases as the square of distance traveled, and also because atmospheric absorption is proportional to path length, the reflectance signal from high-elevation ground is stronger than that from lower elevations. An additional complication is illustrated in figure 3: rays of incident light from the sun are reflected specularly at an emission angle (e) which is equal to the incidence angle (i). Diffuse reflection travels in all directions from the illuminated surface; however, the diffuse light from the surface still peaks near the emission angle. As the sensor picks up light reflected from surfaces whose orientation changes relative to the line-of-sight, the received intensity varies as a complex function of illumination angle, surface orientation, emission angle, and sensor orientation (Hapke, 1993). Finally, sunlight striking a hillside at a grazing angle provides less illumination than sunlight striking level ground at a high angle of incidence; shadowing at low incidence results in additional lost signal. The most intuitive way to regard all of these effects is to consider the final results of spectral analysis. As the signal level decreases and noise remains constant, the relative quality of the signal degrades. This reduces the quality of a spectral match between observations and reference spectra in the spectral library. The final result is decreased confidence in accuracy of identifications for areas of low signal-to-noise. The areas most affected by these geometric variations are the edges of the flightlines, and portions of steep slopes far from and facing away from the aircraft travel path. When interpreting the AVIRIS results, the operator must make allowances for such complications.
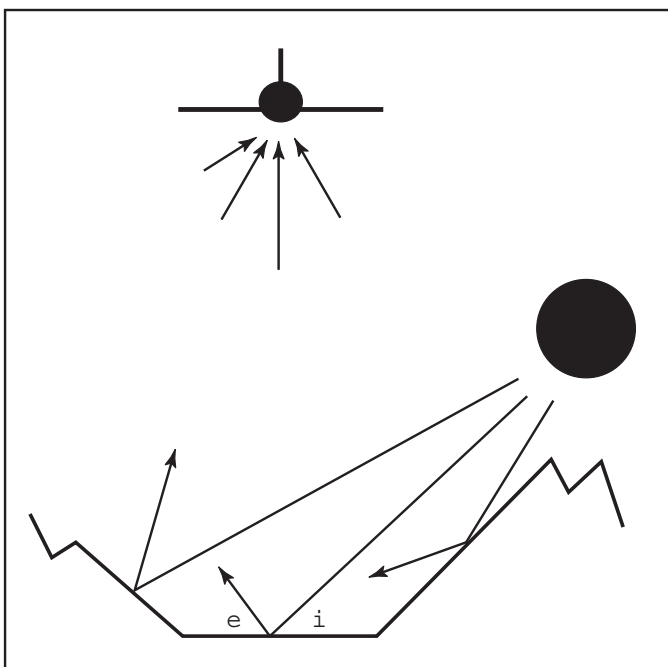

Figure 3. Viewing and illumination geometry for a scene incorporating topographic relief; e, emission angle; i, incidence angle.

Atmospheric Correction

Interferences arising from atmospheric absorptions and wavelength-dependent solar spectral response were corrected using the ATREM atmospheric correction program (Gao and others, 1993, 1997). The ATREM program uses the ratios of water absorption lines in each pixel spectrum to derive an atmospheric column abundance for water vapor. Other species with infrared absorptions such as carbon dioxide and ozone are scaled on the basis of the water values and then ratioed from the final data. Correction of the Animas River watershed data set utilized an average elevation of 3.2 km and a visibility of 200 km. Total ozone column abundance was inferred to be 0.34 atm-cm. The ATREM algorithm estimates the effects of Rayleigh and aerosol scattering in the radiance path, and performs a first-order path length correction accordingly. Although significant water absorption remains in the spectral data at the major water absorption feature locations of 1.49 and 1.9 µm, the remainder of the spectral range appears virtually water-free and is suitable for mineral identifications and mapping.

Ground Calibration Methods

Subsequent to atmospheric removal, the AVIRIS data were corrected to absolute reflectance using a path radiance correction (Clark and others, 1990, 1991; Clark, Swayze, Heidebrecht, and others, 1993; Dalton and others, 1998) and the known spectrum of a ground calibration site (Clark and others, 2002). Review of the AVIRIS data set revealed that the most suitable site for this correction was a spectrally bland, 300×100 m talus slope at 3.6 km elevation on the southeast slopes of Engineer Mountain near Coal Bank Pass. This talus slope is composed primarily of white porphyritic andesite (93–96 percent by area) and a small amount (3–5 percent) of a red sandstone, with sparse (1–2 percent area) lichen and virtually no appreciable absorption features in the AVIRIS spectral range. Field expeditions were conducted to collect upward-facing rock samples from the slope for laboratory analysis. Laboratory measurements were made for 39 collected specimens of talus from Engineer Mountain using a modified Beckman 5270 spectrophotometer. Estimates of rock shadowing (≈15 percent by area) were made from photos taken during the field expedition. Talus spectra were averaged together with a "shadow" component to produce a representative composite spectrum. Additional in-place spectra were later collected using an Analytical Spectral Devices ASD FR-653-1 portable field spectrometer. Three horizontal traverses of the slope were done at different locations on both trips in order to accurately characterize the site. Reflectance values of all measurements were found to be in close agreement. The "path radiance," an estimate of scattered light intercepted by the AVIRIS sensor, was derived using spectra from the AVIRIS image cubes over heavily vegetated, north-facing slopes that were essentially black to the spectrometer. A path radiance correction was derived which brought the

AVIRIS spectra of the Engineer Mountain site into agreement with both the laboratory and field spectra of the site. This path radiance correction was then applied to the entire AVIRIS data set.

Engineering Correction for Platform Motion

Imaging spectrometers mounted on both spacecraft and aircraft must contend with spatial distortions introduced by the motion of the platform. Roll, pitch, and yaw of the platform each introduce specific spatial distortions (Richards, 1994). Velocity variations in the direction of travel, and to a lesser extent, buffeting by crosswinds as well, cause additional distortions for airborne sensors (Sabins, 1987; Richards, 1994). Although the AVIRIS sensor is stabilized by gyroscopes, these distortions still affect the data. The addition of Global Positioning System (GPS) technology to the AVIRIS system has greatly facilitated the process of correcting these geometric distortions. Another geometric problem is known as "smile": since the AVIRIS sensor uses a rotating mirror to direct the field-of-view across a linear strip, there is a difference in path length for light traveling from the edges of the scene as compared to light traveling from the center of the scene, directly below the aircraft. The inverse-square attenuation of light coupled with absorption proportional to path length causes differences in the strength of the received signal and consequent changes in the signal-to-noise ratio proportional to a cosine function across each strip of the image cube.

The AVRECGEN and AVRECTFY programs (Clark and others, 1998) were used to correct all of these distortions. AVRECGEN and AVRECTFY operate on the Tetracorder-processed mineral map images, not on the image cubes themselves. The correction method applies GPS data recorded in flight to each pixel to determine its exact latitude and longitude, and reprojects the final images using a nearest-neighbor interpolation. Because averaging of adjacent spectra destroys the original signal and its associated diagnostic absorption bands, application of the rectification procedures to the image cubes themselves would result in loss of spectral information. Instead, the image cube data are analyzed and interpreted, and the resultant processed images reprojected to a standard mapping base.

Spatial Corrections and Orthorectification

Following the just-mentioned engineering corrections for effects of aircraft motion, the images are much closer to a flat *x-y* plane. Some residual spatial distortions still remain, and the effects of topography must be taken into account. Terrain rectification is needed for the extreme relief displacement found throughout the study area to accurately map the areal extent and location of the various materials found.

Traditional orthorectification processes cannot be used for AVIRIS airborne scanner data because image acquisition is not instantaneous as in aerial photography. Each pixel of each

scan line has a unique geometric model. The traditional orthorectification processes such as polynomial transformations rely on information about camera lens distortions and accurate ground control point locations in *x*, *y*, and *z*. Radial basis functions, such as multiquadric and thin-plate spline, have produced the best results for orthorectification of airborne scanner data (Wiemker and others, 1996; Ehlers, 1994; Ehlers and Fogel, 1994). Two principal characteristics distinguish the multiquadric and thin-plate spline from the polynomial approach: (1) the functions interpolate (the control points match exactly between images) and (2) their behavior is mathematically constrained between control points (Ehlers and Fogel, 1994).

Thin-plate spline functions (Bookstein, 1989) interpolate the values at all ground-control points (GCPs), and a new GCP can be added or deleted where the transformation is not satisfactory. Unlike polynomial transformations that require a small number of points depending on the order of the polynomial, the thin-plate spline may require hundreds of points in rough terrain. There should be a GCP at every extreme of the terrain, peak or valley, and along break lines. Whereas this process requires a large number of control points, there is a fine line between having too many points and not enough. Too many points in a location can actually introduce localized geometric distortions.

A two-step process was used to correct the 17.5-m resolution AVIRIS data using the PCI OrthoEngine v. 6.3 software package. For this project, there were two flightlines to be corrected. Prior to merging, the western flightline was 636 pixels by 3,034 lines and used 234 GCPs. The eastern flightline was 636 pixels by 2,520 lines and used 131 GCPs. Portions of fifteen USGS 1-m digital orthophoto quadrangles (DOQs) were used for reference points. These DOQs formed the foundation for the revision of the hydrography and transportation vector layers and any subsequent fieldwork. Terrain elevations were obtained from USGS 10- and 30-m digital elevation models (DEMs). The bulk of the elevations came from the 10-m DEMs. The first step defined the GCPs using a second-order polynomial transformation which was done to evaluate the selection of the points. Root-mean-square (RMS) errors were normally kept in the 3- to 4-m range with no RMS errors exceeding 10 m. During the second step, each GCP was assigned an elevation from the DEM. After the elevations were assigned to the points, the image correction using the thin-plate spline transformation was performed. This two-step process was similar to the methods used by Ehlers (1994), which followed a global second-degree polynomial transformation with a registration using multiquadric interpolation and a radial basis function.

The registration was checked by selection of points throughout the AVIRIS image and comparison with the same points in the DOQ image. Comparisons of the AVIRIS image were also checked against revised hydrography and transportation vectors. The distances between the revised vector features and DOQs, and the rectified AVIRIS imagery were generally within one to two pixels. The fully orthorectified and georeferenced AVIRIS imagery is suitable for fieldwork, mapping, runoff modeling, and inclusion in GIS databases.

Classification Methodology: The USGS Tetracorder Algorithm

The USGS Tetracorder algorithm is an expert system (Clark and others, 1990, 1991; Clark, Swayze, and Gallagher, 1993; Clark and Swayze, 1995; Dalton and others, 1998; Dalton, 2000; Dalton and others, 2000; Swayze, Smith, and Clark, 2000; Swayze, Smith, Clark, Sutley, and others, 2000; Clark and others, 2003 and references therein) for classification of spectral image cubes on the basis of comparison of unknown spectra with those in a library of reference spectra. Although the Tetracorder system is described fully elsewhere (references in this paragraph), a brief explanation of the methodology is useful here. Tetracorder attempts to duplicate the quantitative and qualitative comparisons performed by a trained spectroscopist. Once supplied with a set of rules corresponding to absorption features in a reference spectral library, the algorithm applies complete band shape least-squares matching criteria to compare each spectrum in the image cube to each spectrum in the reference library.

Infrared Spectral Comparison

The AVIRIS sensor returns measurements of spectral intensity for the visible and near-infrared wavelength range extending from 0.35 to 2.5 µm. Representative spectra for the iron oxide minerals jarosite, goethite, and hematite are shown in figure 4; spectra of muscovite and the clay minerals kaolinite and halloysite are given in figure 5. The materials in each figure exhibit diagnostic spectral absorption features in different wavelength regions. In figure 4, a broad absorption band is evident near 1 µm in all three spectra. This diagnostic absorption arises from crystal field transitions of the Fe^{3+} atom in the molecular structures (Burns, 1993; Clark, 1999) of these three minerals. The left and right edges of this absorption feature relative to the surrounding continuum reflectance levels (fig. 4) differ in each spectrum. For example, the absorption feature is much broader in the jarosite spectrum. The position of the band minimum, the full width at half-maximum, and the relative strengths of the absorptions also vary. These characteristics of the diagnostic Fe^{3+} absorption can be exploited to differentiate between iron-bearing minerals. In similar fashion, the three spectra in figure 5 may be differentiated using their diagnostic absorption features centered around 2.2 µm. These arise from cation-OH vibrational transitions in the mineral matrix. Note that the spectra in figure 5 do not exhibit strong absorption features near 1 µm as with the iron-bearing minerals in figure 4: this is because of differences in their chemical composition. Similarly, the goethite and hematite do not have diagnostic
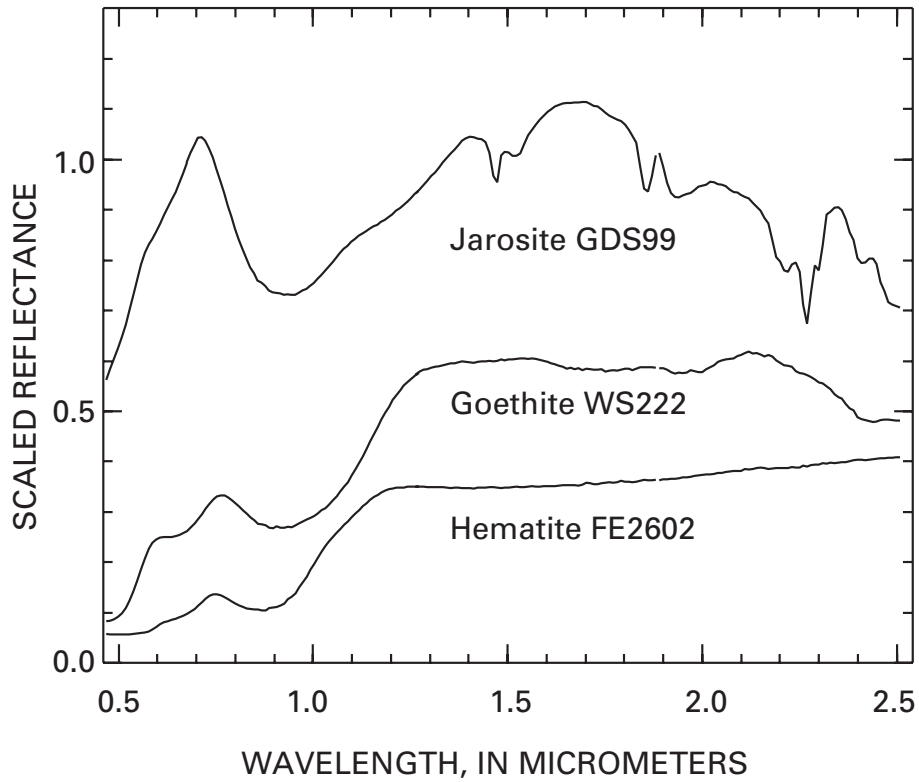
Figure 4. Visible to near-infrared spectra of the iron-bearing minerals jarosite, goethite, and hematite (from Clark, Swayze, Gallagher, and others, 1993). Spectra are offset vertically for clarity. Sample numbers noted after mineral name.
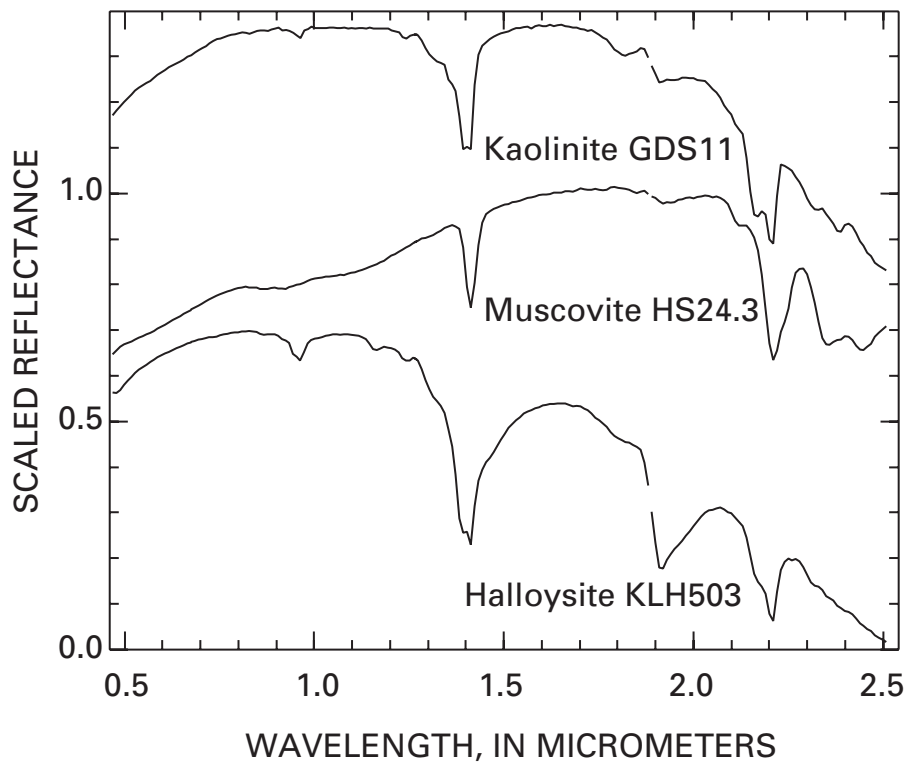

Figure 5. Visible to near-infrared spectra of the alteration products kaolinite, muscovite, and halloysite (from Clark, Swayze, Gallagher, and others, 1993). Spectra are offset vertically for clarity. Sample numbers noted after mineral name.

absorption features in the 2-μm range, although the jarosite, a weathering product, exhibits an Fe-OH absorption at 2.27 μm (fig. 4). Differences occur again in the widths, center positions, and overall shapes of the 2.2-μm diagnostic absorption features in figure 5 which may be used to distinguish between these minerals. Even better, complete band shapes may be compared in a least-squares sense to provide a quantitative discrimination method.

The discrimination of vegetation types proceeds in a similar manner. The spectral behavior of vegetation is dominated by pigments such as chlorophyll and carotene, and the cellular structures composed of cellulose, lignin, and proteins. These common components always absorb at the same wavelengths, though with differing relative strengths and band shapes. The most obvious feature in vegetation spectra is the chlorophyll absorption just short of 0.7 μm in the grass and lichen spectra (arrows, fig. 6). The lichen in this example is a pale-green species (*Xanthoparmelia cumberlandia*), which is common in the San Juan Mountains. Note that the chlorophyll absorption feature is missing in the lower spectrum, of dry (senescent) grass. Absorptions arising from water in the cellular structure can be seen in the green grass spectrum at 1.0, 1.2, 1.45, and 1.9 μm, but are subdued in the lichen and dry grass spectra. A local reflectance peak at 0.55 μm in the green grass highlights the green color of chlorophyll-bearing vegetation, and again it is missing from the dry grass and subdued in the lichen spectrum. The Tetracorder 3.6a2 library includes several vegetation types ranging from grasses, lichens, and ground cover to deciduous and coniferous tree species. A more complete description is given in Clark and others (2003).

All of the minerals shown have weaker absorptions in addition to the diagnostic absorption features discussed. In practice, many of these absorptions may not be used for discrimination between mineral types arising from signal-to-noise issues or interference from other minerals or other materials. For example, the weak absorption feature at 0.65 μm in the goethite spectrum may be completely obscured by noise in an AVIRIS scene and so may not be useful for discrimination. An additional concern is highlighted by noting that each spectrum in figure 5 exhibits absorption features at 1.4 and 1.9 μm arising from water molecules present within the sample. Because the Earth's atmosphere also contains water, AVIRIS spectra are typically overwhelmed by the atmospheric water signature at these wavelengths, even after atmospheric correction. Thus, these absorption features cannot be exploited for mineral identification. Another example is the 2.27-μm absorption in the jarosite spectrum: because of its proximity to the clay and mica absorption features, and because jarosite is an alteration product which often occurs together with several clays, this absorption feature is frequently unusable for identification of jarosite.

The complex interplay of spectral behavior among materials that sometimes occur together in the same scenes is embodied in a set of decision rules. The USGS Tetracorder 3.6a2 implementation is the result of several years' experimentation

to derive the best criteria for simultaneous, automated discrimination of multiple mineral types. The following sections discuss this approach in greater detail.

Continuum Removal and Band-Fitting Methodology

Whereas the full spectrum may not always be useful for spectral discrimination, diagnostic absorption features can usually be specified for each material, which can be applied to uniquely identify that material. The USGS Tetracorder algorithm, as an expert system, relies on user interaction to define the diagnostic absorption features to be used for each material under consideration. Because in practice the observed spectrum will usually be of a mixture of materials, rather than a pure material, the algorithm uses a continuum-removal scheme (Clark and Roush, 1984) to minimize the spectral contributions from other materials in the scene.

All materials in an AVIRIS pixel, whether mineral, vegetation, water, or other substances, contribute to the total reflectance spectrum measured by the instrument. In an idealized case, each material could be considered to exhibit spectral behavior only in the region of a strong absorption band. Hematite (fig. 4) displays little structure outside the primary absorption features at 0.46 and 0.85 μm other than a gradual slope. The kaolinite spectrum in figure 5 is nearly level to either side of the 1.4-μm water absorption feature. Other materials may depart from such idealized behavior, as with jarosite (fig. 4); still, each absorption feature can be seen as superimposed upon an overall reflectance level defined by the edges of the absorption feature. Each AVIRIS pixel can realistically be expected to contain several materials. Averaging over the spectral contributions of all these materials produces a continuum that can be modeled as a background reflectance level approximated by a straight line. Removing continuum effects in the vicinity of diagnostic absorptions allows individual absorption features to be compared to those of a reference material with a minimum of interference.

The method is illustrated in figure 7. For a given reference material having a diagnostic absorption feature spanning a set of wavelengths (λ), a library spectrum $L(\lambda)$ is examined interactively by the operator (fig. 7A). Anchor points are defined as the wavelengths bounding the absorption feature; this sometimes requires a reasonable working knowledge of spectroscopy and the materials of interest. A straight line $C_L(\lambda)$ is fit to the anchor points and considered to approximate the continuum across the absorption feature in spectrum $L(\lambda)$. During automated comparison, each observed spectrum $O(\lambda)$ is compared to every spectrum in the reference library. For each diagnostic absorption feature, a continuum level $C_O(\lambda)$ is calculated for the observed spectrum using the anchor points of the library spectrum $L(\lambda)$. The anchor points from the library spectrum, and not the observed spectrum, are used for three reasons. First, the

library spectrum generally has better signal-to-noise and consequently produces improved wavelength estimates. Second, determination of anchor points is time consuming. Third, the observed spectrum can vary with composition, viewing geometry, scattered light, and other factors, which could result in different anchor points for each spectrum. This complicates the automated comparison. In the case where the reference material is not present in the observation, any mismatch of anchor points is of secondary concern because the spectra are not likely to match anyway, so the material will be rejected.

The next step (fig. 7B) is to divide each spectrum by its corresponding straight line continuum to produce the continuum-removed spectra, $L_C(\lambda)$ and $O_C(\lambda)$, corresponding to the library and observed spectra, respectively. The apparent depth D of an absorption feature relative to the surrounding continuum in a reflectance spectrum (Clark and Roush, 1984) is given by

$$D = 1 - \frac{R_b}{R_c}, \qquad (1)$$

where R_b is the reflectance at the absorption band center wavelength λ_{bc} and R_c is the reflectance value of the continuum $C(\lambda)$ at the band center wavelength. The band center wavelength λ_{bc} is found by locating the band minimum in the continuum-removed feature, as in figure 7B. The reason for using the continuum-removed feature to choose the wavelength rather than the raw spectrum is to remove the influences of other materials contributing to the spectrum. Because the depths of absorption features change with the abundance of a material, the strength of each absorption feature must be scaled, without changing its spectral shape, in order to compare the strong spectral absorption features of pure reference materials with features in the observed spectra where abundances may be much lower. After continuum removal, the Tetracorder algorithm adjusts the library spectrum absorption feature depth to match the depth of the observed spectral absorption feature (fig. 7C). This is done through a modified least-squares approach, and the goodness-of-fit estimated for the best match in spectral contrast is the value used for the later decision-making routines. The modified least-squares technique, originally outlined in Clark and others (1990) and further developed in Clark, Swayze, and Gallagher (1993), Clark and Swayze (1995), and Clark and others
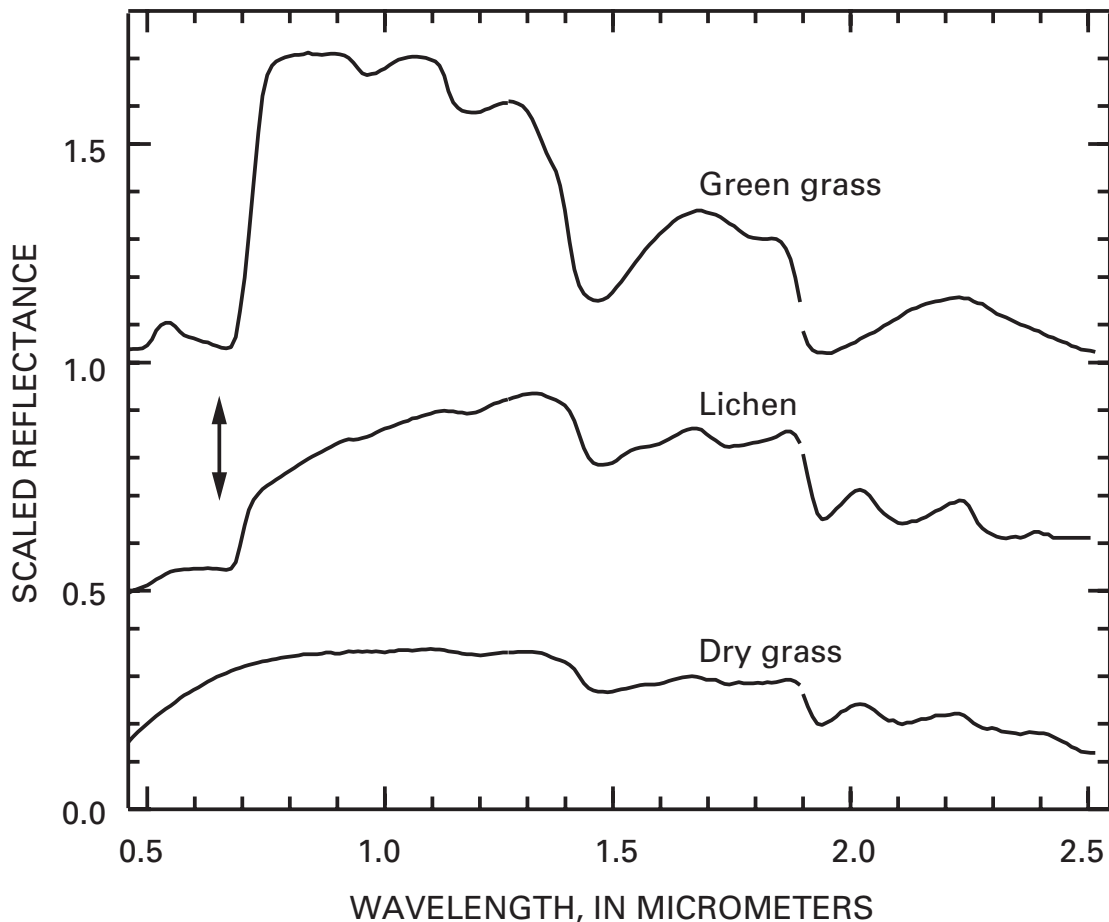
Figure 6.   Visible to near-infrared spectra of green (lawn) grass, lichen (*Xanthoparmelia cumberlandia*), and dry, senescent grass. The grass spectra are from Clark, Swayze, Gallagher, and others (1993), whereas the lichen was measured as part of this study. Arrows mark the location of principal chlorophyll absorption feature in the upper two spectra, which is not apparent in the dry grass spectrum.
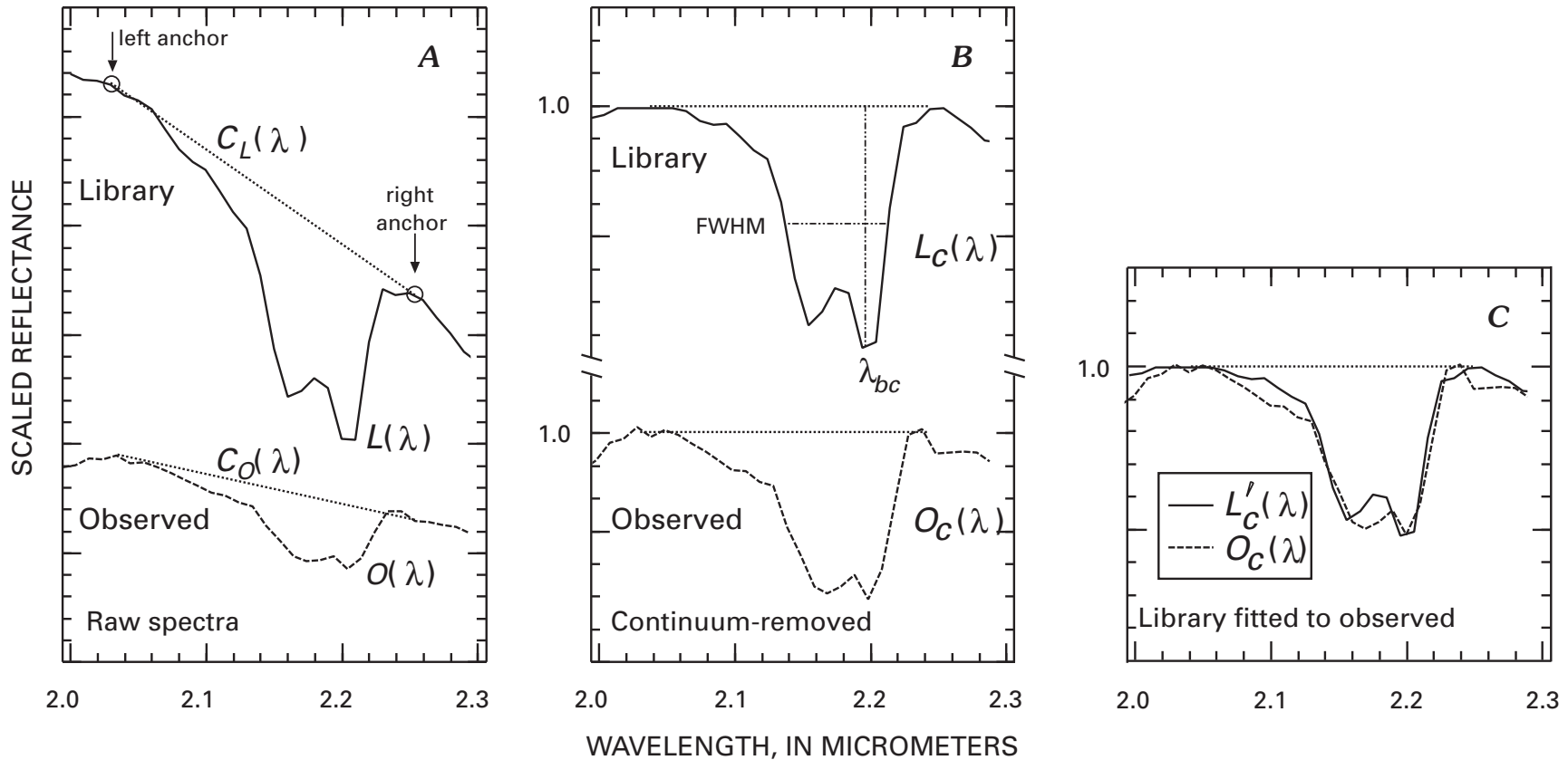
Figure 7. Continuum-removal and band-fitting procedure as used by Tetracorder algorithm. *A*, Anchor points are defined utilizing an absorption feature in a library reference spectrum of known material. A straight-line continuum is then fit to both the library and observed spectra. *B*, Each spectrum is divided by its continuum at all wavelengths. The band center wavelength is determined from the continuum-removed library spectrum. *C*, The spectral contrast of the library spectrum is adjusted to match that of the observed spectrum to facilitate comparison by least-squares methods. The correlation coefficient calculated for the adjusted spectral absorption features is used as input to other routines of the Tetracorder system. Modified from Clark and Roush (1984), Clark and others (1990), and Dalton (2000). FWHM is full width at half maximum.

(2003), accomplishes this without iteration through a succinct and computationally efficient enhancement to the standard least-squares equations described in Bevington (1992). The method is summarized in Dalton (2000) and described fully in Clark and others (2003). Briefly, the continuum-removed reflectance values at all wavelengths within the anchor points are used to determine a scaling which minimizes the differences between the continuum-removed library and observed spectra. The resultant scaled, continuum-removed library spectrum $L'_C(\lambda)$ gives the closest possible match to the observed spectrum, and its correlation coefficient r estimates the quality of the match.

Each observed spectrum in the image cube is compared to all components of the reference library. For each material under consideration, the Tetracorder algorithm produces three values. The goodness-of-fit, F, is just the correlation coefficient r, and measures how well a material matches the observed spectrum. The depth D of the absorption feature is indicative of the abundance of that material in the scene. Although D is also sensitive to grain size variations, in general the changes in composition are much more important (Hapke, 1993). At constant grain size, D roughly corresponds to relative abundance changes throughout a given scene (Lucey and Clark, 1985). Combining the fit and depth by multiplying $[F \cdot D]$ provides a more robust estimate of relative abundance (Clark and others, 1990, 2003). Using this value helps to avoid confusion arising from noise, other materials having absorptions at similar wavelengths, and situations where a low abundance of one material is accompanied by a high abundance of another.

In the simplest case, a material will have a single absorption feature, which is compared to the observed spectrum. Spectra of some materials may have multiple spectral absorption features, which can be used for identification. The Tetracorder algorithm can be instructed to use the relative areas of individual absorption features in a single reference spectrum to compute a weighted fit F_w, weighted depth, D_w, and weighted fit times depth $[F \cdot D]_w$ which is used in the decision process. If c_i is the area of the ith absorption feature relative to the continuum, then the weighted fit, weighted depth, and weighted (fit times depth) are defined as:

$$F_w = \sum_{i=1}^{w} c_i F_i \tag{2}$$

$$D_w = \sum_{i=1}^{w} c_i D_i \quad \text{and} \tag{3}$$

$$[F \cdot D]_w = \sum_{i=1}^{w} c_i F_i D_i \tag{4}$$

where $\quad \sum_{i=1}^{w} c_i = 1.0 \tag{5}$

and the absorption feature depths and weights are computed from the fitted, continuum-removed library reference features to minimize effects of noise and other materials in the scene (Clark and others, 1990; Dalton, 2000; Clark and others, 2003).

Once the weighted fit (F_w), depth (D_w), and their product $[F \cdot D]_w$ values have been generated, the operator-specified rules are applied. At its most basic, Tetracorder declares the reference material having the highest F_w or $[F \cdot D]_w$ value to match the observed spectrum. However, more advanced logic can be applied. For example, Tetracorder may be instructed to reject a mineral assignment if a strong chlorophyll absorption feature is found. This would mean that the observed spectrum is in fact caused by vegetation. These "NOT" features may be defined for any material, and are particularly helpful in cases where certain materials have similar or overlapping absorption features but one material has a characteristic absorption feature which can be used for discrimination. Another approach is to group certain materials and compete them against each other in subclasses. One example is the grouping of iron oxides, which are characterized by strong electronic transitions in the 1-µm range (Group 1); another would be grouping of the clay minerals, which exhibit vibrational absorptions in the 2.2-µm range (Group 2); a third grouping would be that of vegetation types, all of which would display chlorophyll-related absorption features near 0.7 µm.

Materials within each group are competed against each other to select the best fit. For each material, three processed images are generated from the AVIRIS data. The intensity values of each pixel in these three images correspond to the weighted fit (F_w), depth (D_w), and fit times depth $[F \cdot D]_w$ for the reference material class under consideration. A clustering algorithm prioritizes output images on the basis of the size of contiguous regions of high pixel values. The operator examines these images and assembles them into color-coded maps of material distributions. For this investigation, only materials having $[F \cdot D]$ values above a given threshold are displayed. Values above the threshold are all assigned the same intensity in the final images. The threshold was determined individually for each material by the operator, based not only on the quality of the fit and the spectral data, but also on results of field studies. The variable extent of operator involvement is one factor in the characterization of the Tetracorder as an expert system.

To discriminate goethite from hematite, the algorithm compares the fit values for the primary diagnostic absorption features centered near 1.0 µm (fig. 4). Though subtle to the eye, the different shapes produce substantially different correlation coefficients when least-squares calculations are performed for the full band shape. Similarly, the 2.2-µm absorption features of halloysite and kaolinite (fig. 5) are compared directly for discrimination. In the case of muscovite, this absorption feature is supplemented by a second feature near 2.3 µm for a more robust discrimination. Jarosite is treated somewhat differently: the 0.43-µm and 0.91-µm absorption features are competed against the 1-µm absorption features of the other iron oxides and Group 1 minerals, but the 2.27-µm absorption is not used to supplement this. Rather, the 2.27-µm absorption feature is utilized in a separate grouping, with the clays, carbonates, and other Group 2 minerals, to prevent misidentifications in that spectral range. The reason that the jarosite absorption features in both spectral ranges are not used together is that whereas the shorter-wavelength absorption features are quite strong, the 2.27-µm absorption is not as strong when compared to the clay and carbonate minerals which exhibit diagnostic absorption features in that portion

of the spectrum. This could cause jarosite to be ruled out in some cases where it is present, or where it is inaccurately assigned to pixels containing mixtures of clays, carbonates, and iron oxides. Such knowledge of the spectral characteristics of the materials expected in a scene is crucial to the correct implementation of Tetracorder identification strategies.

Potential Sources of Error

The researcher must take some precautions when interpreting the processed AVIRIS images. First, the value [$F \cdot D$] is not a strictly valid abundance estimator. A material having strong absorption features may dominate the spectrum despite the presence of other compounds. Certain minerals are virtually featureless in the near infrared: quartz has no strong absorption features in the AVIRIS spectral range, whereas pyrite is so strongly absorbing that its spectrum is merely a flat continuum. In mixtures, these two minerals cannot be discriminated. The identification of a given mineral in a certain pixel must not be taken to mean that it is the only material present. Conversely, the absence of a material in the final images does not mean that it is not present.

Variations in signal-to-noise ratios give rise to additional concerns. For example, where two materials have spectral absorption features, changes in noise levels can influence the spectral match so that one material is chosen over the other. In areas where shade cover or surface orientation changes rapidly, this can result in mineral identifications which alternate between spectrally similar materials. In some cases, a material may spectrally dominate a pixel despite the presence of other, more abundant components. Spurious identifications also may occur because of fluctuations in noise levels. Regions of low signal, such as shadowed areas, north-facing slopes, and dark or wet rocks in particular may produce such spurious identifications. Near the edges of the flightlines, increased path length results in reduced signal levels. Although all mineral identifications presented in this report have been spot-checked in the field to verify accuracy, only major and easily accessible target areas have been visited because of the large size and extreme ruggedness of the study area. In general, large areas of a given material identification should be considered more trustworthy, whereas a single-pixel identification with no neighbors must be treated with caution.

Similar Mineral Signatures: Calcite, Epidote, and Chlorite (CEC)

Special attention must be paid to minerals having highly similar spectra, including calcite, epidote, and chlorite. The distribution of calcite is important herein because of calcite's ability to neutralize acidic waters resulting from pyrite weathering and acid mine drainage (Church and others, 2000). Chlorite also has some acid-neutralizing potential (Desborough and others, 1998), although it is an order of magnitude less than that of calcite. Limestone occurs throughout the sedimentary

units in the lower Animas River area south of the Silverton caldera, and these units were readily identified using the Tetracorder 3.4a8 implementation (Dalton and others, 1998). Calcite-bearing propylitic alteration zones containing abundant epidote and chlorite also occur within the caldera region and may also produce significant neutralization of acidic water (Bove and others, 2000; Dalton and others, 2000).

Progress in mapping the extent and composition of these zones was hampered by the spectral similarity of the diagnostic bands of calcite, epidote, and chlorite (fig. 8; Dalton and others, 1998, 2000, 2002, 2004). Although the pure end members are readily distinguished, the identical band center positions make it difficult to correctly identify mixtures of these three minerals. Most perplexing is that mixtures of chlorite and epidote containing no calcite mimic the calcite spectral signature quite closely. The bottom spectrum in figure 8 is of a rock collected in the field. This sample (SJ98-74D) is a fine-grained, propylitically altered igneous rock containing abundant epidote (approximately 45 percent) intimately mixed with about 7 percent calcite and 11 percent chlorite, as determined by point counts. As it
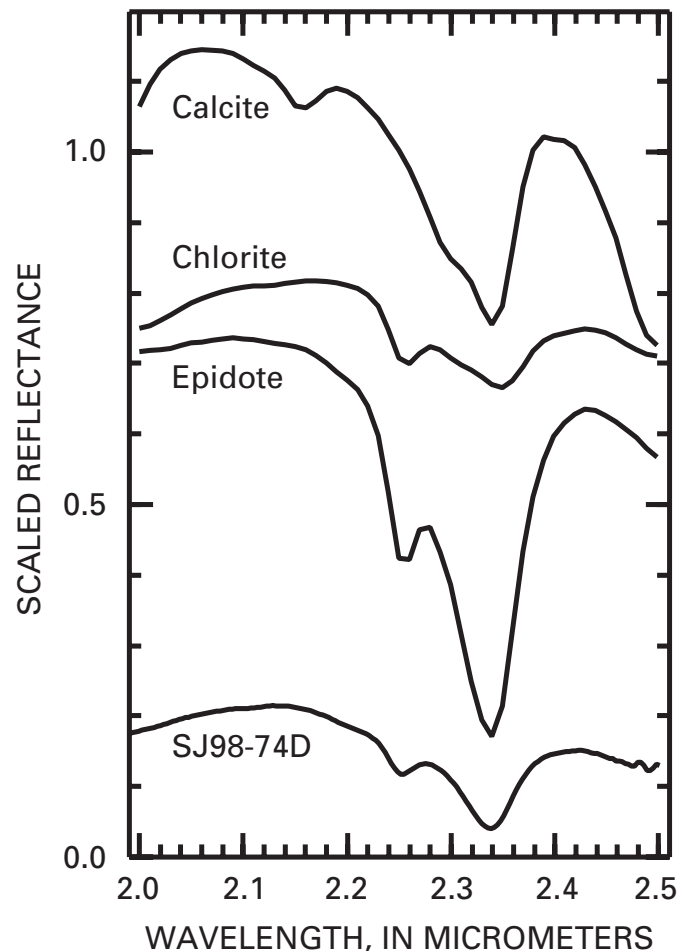

Figure 8.   Diagnostic spectral absorptions of calcite, chlorite, and epidote in the 2-μm region. Field sample SJ98-74D is a fine-grained mixture of all three (Dalton and others, 2002).

is an intimate mixture, its spectrum is not merely a linear weighted average of the spectra of its components. This made theoretical modeling of mixture spectra virtually intractable, and as the relative proportions of these three minerals change throughout the propylitic alteration zones, mapping the distribution of these particular minerals was not straightforward.

As described in Dalton and others (1998, 2002, 2004), the identification of mixtures containing these three minerals was accomplished by collecting samples of the pure end members, grinding and sieving them in the laboratory, and mixing them in various proportions. The spectra of these laboratory mixtures were measured under controlled conditions and then added to the Tetracorder reference library. Once the continuum anchor points were defined, the Tetracorder system was able to categorize the three end members (including calcite as limestone) from mixtures of two or three components. The method also separated the results into classes dominated by one or another component. Computation of more precise, quantitative unmixing and abundance estimates were, however, deemed prohibitively expensive at the time.

A further complication arose concerning the presence of sericite within the propylitic zones of the study area. The petrographic name sericite is a general name used by field geologists to describe highly birefringent, fine-grained micas found in the vicinity of hydrothermal mineral deposits (Meyer and Hemley, 1967). This term has been loosely applied over time, and can include muscovite $(KAl_2(Si_2Al)O_{10}(OH,F)_2)$, paragonite $(NaAl_2(Si_3Al)O_{10}(OH)_2)$, and potassium-bearing, poorly crystalline, disordered micas such as illite $[(K,H_3O)(Al,Mg,Fe)_2(Si,Al)_4O_{10}((OH)_2 \cdot H_2O)]$ (Fleischer and Mandarino, 1995). These are all compositionally and structurally quite similar (Klein and Hurlbut, 1993), particularly with regard to the position of the hydroxyl components, and their spectra as a result are also similar, especially in the 2-μm range, which is most sensitive to hydroxyl vibrational transitions (Hunt and others, 1973; Hunt and Ashley, 1979). For example, muscovite (fig. 5) exhibits spectral behavior arising from the presence of hydroxyl at 2.2 and 2.3 μm. The positions and relative strengths of these absorptions are very close to those in paragonite and illite (Hunt and Ashley, 1979; Clark, Swayze, Gallagher, and others, 1993). Whereas virtually all of the sericite encountered in the field during this study was determined by X-ray diffraction analysis to be illite (Bove and others, 2000), the spectral similarities within the class and the level of discrimination achieved by the Tetracorder 3.6a2 system, coupled with limited field coverage, precluded confident assignment of all sericite identified by the Tetracorder analysis as illite. Hence, in this report the term sericite will be used in its general sense, with the understanding that illite is the most abundant form in the region (see, for example, Eberl and others, 1987) and the most likely to be encountered on the ground.

Where calcite, epidote, and chlorite occur together with sericite (illite), the 2.3-μm hydroxyl absorption feature in the sericite spectra (see, for example, muscovite in fig. 5) interferes with the comparisons of the 2.3-μm absorption features

of the calcite, chlorite, and epidote. Fortunately, the 2.2-μm absorption band is readily distinguished, and so pixels containing sericite in combination with calcite, epidote, and (or) chlorite have been identified. More detailed interpretation of these spectra is not yet possible without a comprehensive laboratory investigation of the same type reported in Dalton and others (2004), but for the six minerals (muscovite, illite, paragonite, calcite, epidote, and chlorite) and combinations thereof, rather than three (calcite, epidote, and chlorite). Such a study would be valuable in extending the capabilities of remote sensing for characterization of hydrothermal alteration systems. Nevertheless, useful results have been obtained by grouping mixtures of these materials into categories establishing a primary mineral phase where possible. Breakdown of the various classifications into color-coded images is described further in the next section, with the specific detail of the calcite-epidote-chlorite distributions in the subsection on acid-generating and acid-neutralizing mineral assemblages.

Tetracorder Results for the Animas River Watershed

The spatial and spectral analysis of the Animas River watershed AVIRIS data concentrated on five general regions of the watershed and separated the spectral information into four broad classes. Note that as more than one material may be present in a given pixel, it is not possible to show all of the materials in a single image. Additionally, there are far more "colors" in the infrared than can be discerned by the human eye using the visible range, and so it makes more sense to present the information in a series of separate images, which also enables multiple coexisting materials to be depicted. The spatial regions within the caldera and farther downstream have markedly different characters, and thus are described separately. In the spectral domain, the first two classes (iron oxides and alteration products) are defined by broad mineral groups having their infrared absorptions in different wavelength ranges: Group 1 absorbing in the 1-μm range, and Group 2 in the 2-μm range. The last three spectral classes are defined in terms of end-user interests (vegetation types and water-quality issues). Group 3 includes vegetation and snow; Groups 4 and 5 are acid-generating and acid-neutralizing minerals. The Tetracorder algorithm is capable of separating hundreds of materials. The results presented in this report are confined to those relevant to the scope of this study.

Group 1: Iron Oxide Family

The Fe^{3+} and Fe^{2+} crystal field transitions near 1 μm provide a convenient method of discriminating iron-bearing minerals through infrared spectroscopy. Because the exact wavelength positions and spectral shapes of the absorptions are strongly affected by the crystal structures hosting the iron

atoms, many minerals have distinctive spectra in this range that are easily discriminated by the least-squares shape fitting approach of the Tetracorder system. In some cases, the 1-μm spectral comparisons were supplemented with information from the 2-μm range for a more robust identification.

Of greatest importance to this study are the pyrite (FeS_2) oxidation assemblage products. Goethite ($FeO(OH)$), hematite (α-Fe_2O_3), maghemite (γ-Fe_2O_3) and schwertmannite ($Fe_8O_8(OH)_6SO_4$) are easily discriminated by spectral comparisons, and they tend to occur in concentric zones associated with pyrite weathering (Swayze, Smith, and Clark, 2000; Swayze, Smith, Clark, Sutley, and others, 2000). Very little maghemite and schwertmannite were identified spectrally in the Animas River watershed, although schwertmannite is a fairly common secondary mineral along stream reaches (Desborough and others, 1998). Pyrite itself, as mentioned earlier, is difficult to detect spectrally, but the iron sulfate jarosite ($K_2Fe^{3+}_6(SO_4)_4(OH)_{12}$) is easily identified and stands as a proxy for some of the most highly concentrated exposures of pyrite (Swayze, Smith, and Clark, 2000; Swayze, Smith, Clark, Sutley, and others, 2000). Because the hematite spectrum is strongly affected by grain size, it was possible to separate fine-grained nanocrystalline hematite from the more common coarser grained variety. Coarser grained specular hematite occurs in the Sultan Mountain stock (Yager and Bove, 2002).

Several other Fe^{3+}-bearing minerals found within the study area have absorption features in the 1-μm range, but their spectra are too similar to fully separate one from another. An additional suite of Fe^{2+}-bearing minerals were found to be widely distributed in the region. Although these Fe^{2+}-bearing minerals fall into roughly four classes, further discrimination is not yet possible. One class is spectrally similar to hematites; others have amorphous, poorly crystalline structures. The spectral differences among these materials are detailed (Clark and others, 2003) and yet of limited interest; thus they will be omitted here. The Fe^{2+} minerals as discerned from the 1-μm spectral region are quite useful in that they tend to differentiate weakly altered rock from intensely altered and pyritic rock. Field mapping within the study area demonstrates that propylitic to weak sericite-pyrite altered rocks typically map as Fe^{2+}-bearing minerals in the 1-μm region (characterized by an illite-dominated spectral signature). This generally reflects oxidation of primary Fe-Ti oxide minerals such as ilmenite and magnetite. In contrast, more intensely altered rock of the quartz-sericite-pyrite assemblage, which may also map as illite-dominant, tends to correlate well with Fe^{3+}-bearing minerals produced by weathering of pyrite, such as goethite and jarosite. Also of interest, these materials, along with amorphous iron oxides, ferrihydrites (such as, $5Fe_2O_3 \cdot 9H_2O$), and amorphous iron hydroxides, have been identified along stream reaches of the Animas River watershed and are believed to have precipitated from metal-rich acidic stream waters (Dalton and others, 2000; Church and others, 2000; Schemel and others, 2000). However, because the affected zones along streams tend to be small fractions of the AVIRIS

pixel size, spectral identification of these precipitates is impeded by their low relative contribution to the collected radiation field.

Although plagioclase is difficult to detect spectrally because of its lack of strong VNIR (very near infrared) absorption features, it is a primary rock-forming mineral and common in volcanic rocks. Where found, it has been included in the AVIRIS images. It is much more prevalent than the images indicate, and so its absence in the images should not be interpreted to mean that it is not present on the ground. Rather, the weak spectral signature of plagioclase is easily overshadowed by other minerals. The images detailing iron oxide distributions also include epidote and some chlorite identified on the basis of 1-μm spectral comparisons. The distributions of epidote and chlorite should be considered as supplemental data to the more complete Group 5 distributions derived from 2-μm spectral comparisons.

Group 2: Alteration Products

Many of the minerals associated with hydrothermal alteration exhibit diagnostic absorption features in the 2-μm range of the infrared spectrum. As with the iron oxides, these minerals tend to occur in roughly concentric zones about a central area in which alteration was most intense. At progressively greater distances from the center zone, the intensity of alteration generally decreases (Rose and Burt, 1979; Sabins, 1987; Bove and others, 2000; Yager and others, 2000) resulting in different mineral products. Because of structural and geologic complexities, the eventual surface expression of such alteration does not generally present itself as neat, perfect "bullseyes," but the overall trend is commonly observed in the field (Swayze, Smith, and Clark, 2000; Swayze, Smith, Clark, Sutley, and others, 2000). In areas of sparse vegetation this is more evident.

Sulfide minerals in acid-sulfate systems are usually deposited in a breccia-hosted silicic zone dominated by sub-stantial quartz and smaller amounts of alunite and kaolinite (Luedke and Burbank, 1966; Fisher and Leedy, 1973; Ashley, 1974). Sodium and potassium alunite may be discriminated spectrally, and they are given separate colors in the AVIRIS mineral maps. Beyond the silicic zone commonly is a zone of argillic alteration which hosts many clays, including kaolinite, halloysite, dickite, and pyrophyllite, along with minor alunite (Meyer and Hemley, 1967). Smectitic clays are commonly found along the periphery of this zone and grade outward into propylitic-altered zones, in which chlorite, epidote, and calcite are abundant (Meyer and Hemley, 1967; Sabins, 1987). All of these materials have spectral absorption features in the 2-μm range and are important to interpretation of the AVIRIS mineral maps. Sericite is also found in argillic, quartz-sericite-pyrite (QSP), and propylitic zones, often as illite, muscovite, or paragonite. Most of the sericite encountered in the Animas River watershed during this study has been in the form of illite (Eberl and others, 1987; Bove and others, 2000). The spectral behavior of

sericite (see, for example, muscovite in fig. 5) in the 2-µm range includes some overlap with absorption features diagnostic of alunites, kaolinite, pyrophyllite, calcite, epidote, and chlorite (fig. 8). In some areas where all these occur together, the Tetracorder system merely identifies the presence of a mixture (such as sericite with alunite and kaolinite) rather than attempt a computationally expensive and likely error-prone quantitative unmixing. Some of these identifications rely upon empirical laboratory mixtures created under controlled conditions and included in the reference library, as was done in the case of calcite, epidote, and chlorite.

Group 3: Snow and Vegetation Distributions

Exposed rock makes up a very small percentage of the study area. Because of the high annual precipitation, the San Juan Mountains are widely vegetated. Additionally, at the time of the AVIRIS overflight, significant snow cover remained. The Tetracorder 3.6a2 reference library contains spectra representative of snow in a range of conditions. Fine-grained frozen snow, medium-grained snow, and partially melted snow are included along with snow-water mixtures and slush. Vegetation spectra representative of lichen (fig. 6), conifers (such as fir, spruce, and pine), deciduous species (aspen, willow, maple), grasses, and crops (alfalfa, wheat) are all included in the library. As the primary focus of this study was to document the effects of historical mining, only broad classes of vegetation and snow cover appear in this report. Whereas these general vegetation maps should be useful to many, their inclusion in this report also demonstrates that minerals were not identified in large portions of the study area because these were covered by vegetation. Field analysis and geologic interpretation are necessary in order to interpolate over these heavily vegetated sites. (See Bove and others, 2001, for more information.)

Most areas of the Animas River watershed contributing significantly to acidic mine drainage are so heavily mineralized that little or no vegetation occurs on them. The presence or absence of vegetation serves as an indicator of soil and water quality. Dry or senescent vegetation is readily identified. Vegetation with dew or rainfall on it has a unique spectral signature—a combination of the water signal and a vegetation spectrum; similarly, snow and vegetation combine to give a unique signal that was identified in certain regions of the study area. Further discrimination of vegetation species in the watershed could prove interesting as well as useful for certain land-management applications.

Groups 4 and 5: Acid-Generating and Acid-Neutralizing Mineral Assemblages

The specific iron oxides associated with pyrite oxidation have been assembled into a separate image on the basis of their importance as indicators of potential sources of acidic drainage. Similarly, the calcite-epidote-chlorite distributions have been assembled into their own image for future assessment of acid-neutralizing potential. The end members calcite, epidote, chlorite, and sericite are identified wherever they dominate the spectrum. In neighboring areas where the end members have decreased in abundance to the extent that they no longer dominate, mixtures of two and three mineral components are identified; in many cases, the primary component is separable, but where all three are present the images do not distinguish the abundances of the lesser two phases. Although the Tetracorder output from which the images in this report were assembled is much more detailed, space and cost limitations prevent publication of the intermediate results. Where sericite is dominant, relative abundances of accessory calcite, epidote, and chlorite could not be ascertained with sufficient confidence to warrant inclusion in the report; interpretations utilizing the images included here should take this uncertainty into account.

Imaging Spectroscopy Tour of Study Area

The digital images provided with this report can best be utilized if first examined in the context of a brief tour. The five broad material classes just described each correspond to a fully processed, orthorectified image mosaic included with this report. Five separate regions of the watershed (fig. 2, areas A–E) have been selected for this tour. They range from the most highly altered portions of the Silverton caldera, through surrounding igneous and sedimentary formations, to the heavily vegetated region near Hermosa. Examination of each of these five regions provides an opportunity to discuss the significant features of each, and provides an introduction to the application of remote sensing in this context. In this fashion, a general familiarity with the data set may be developed from which to expand into other related studies. As the distributions of materials in each of the five classes change from region to region, inferences can be drawn about the underlying mineralogy, ecology, water quality, and other aspects of the study area, from a watershed perspective.

Ironton and Red Mountain Scenes

The Ironton and Red Mountain area (inset A, fig. 2) exhibits most of the salient characteristics of the study area and will be examined in detail. The scenes are dominated by Red Mountains #1–3, which are near the northwest margin of the Silverton caldera. Heavily mineralized, the Red Mountains were actively mined for nearly a century. It is helpful to compare photographs to the AVIRIS mineral maps in order to get a sense of scale and placement. Figures 9, 10, and 11 are photographs taken from the peak of Red Mountain #3 in 1998. Colorado Highway 550 (fig. 12) is discernible in both the photographs and the AVIRIS mineral maps (figs. 13–17).

Figure 9.   Photograph from Red Mountain #3 facing northwest toward Imogene Basin. Colorado Highway 550 is in foreground, with Governor Gulch just right of center and Galena Lion Gulch to the right. These two exposures stand out clearly in figures 11-14. Hayden Mountain is rightmost peak at top of photograph.

Figure 10.   Photograph from peak of Red Mountain #3 facing north toward Crystal Lake and Ironton Park. Colorado Highway 550 passes through valley below Hayden Mountain on left. Ridge on lower right is Red Mountain #2. The brightly colored, weathered rocks of Red Mountain #2 (and #3 in the foreground) contain abundant goethite and jarosite.

In the AVIRIS mineral maps, Crystal Lake is in the upper right corner. The mountains beyond Crystal Lake in figure 10 are outside the range of figures 13–17 but are apparent in figure 1 and in the full image mosaics. Hayden Mountain is to the west of Highway 550 and Red Mountain Creek. Exposed rock along Monument Gulch near the center of figure 10 is dominated by goethite (green) in figure 13, and by kaolinite and sericite (yellow-green, bright rose) in figure 14.

The slopes of Red Mountain are colored with various shades of red, orange, and yellow associated with goethite, hematite, and jarosite on the slopes. Examination of figure 13 reveals a very close correspondence between the AVIRIS mineral map and the visible colors in the photographs (figs. 9–11). Tree patterns on the slopes of Red Mountain in figures 10 and 11 can be used to orient oneself along the mountain. Although the iron oxides have absorption bands extending into the visible, which allow them to be distinguished by eye, the minerals in figure 14 do not show an obvious color correlation in all cases. This is because the clays, sericites, and other alteration products shown in figure 14 have infrared signatures in the 2.0-μm range, but no distinct color in the visible portion of the spectrum. Pure samples are predominantly gray and white. Two large exposures, along Governor and Galena Lion Gulches (fig. 9, lower left; see also fig. 12), are mostly gray and brown rocks, which appear similar, but the mineral maps in figures 13 and 14 clearly distinguish iron oxides, clays, and micas. This should further clarify the reason for separate maps to illustrate the distributions of different mineral groups.
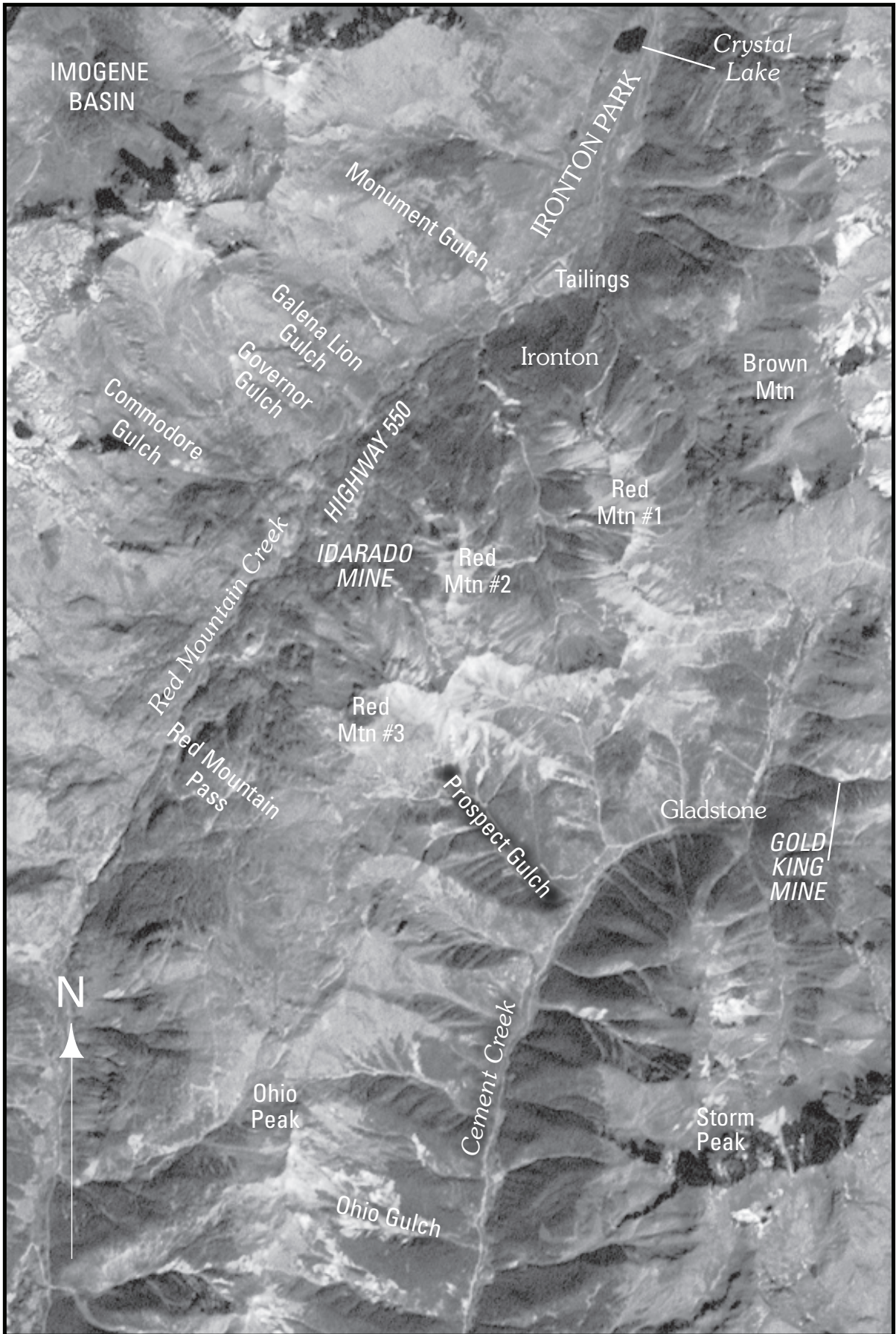
As described in the previous sections, the Tetracorder method does not provide quantitative abundance estimates for mixtures of minerals. However, it can determine when one material is spectrally dominant compared to others. In the explanation to figure 14, for example, "Kaolinite **and** alunite" is denoted by a light orange, whereas a darker orange is used for "Alunite **with** pyrophyllite." In the former case, the kaolinite and alunite occur in roughly equivalent proportions, so the color is assigned to kaolinite **and** alunite, more or less equally. The term "Alunite **with** pyrophyllite" on the other hand is meant to imply that the minerals denoted by the dark-orange pixels are predominantly alunite, **with** some pyrophyllite. Similar logic applies to mixtures of three or more minerals. "Alunite **with** sericite and (or) pyrophyllite" means that alunite is dominant, but there may be either sericite or pyrophyllite, or both, present as well. Sorting out the relative abundances of the minor mineral components may prove intractable in some of these cases.

The general shape of the Silverton caldera can be discerned from the concentration of mineralized zones about the primary hydrothermal alteration zones. The reds and oranges

Figure 12 (following page).   Major geographic features of Ironton Park and Red Mountain region (inset A, fig. 2) as described in text.

Figure 11.   Photograph from Red Mountain #3 facing northeast. Brown Mountain dominates background, with Red Mountain #1 directly in front of it. The ridge of Red Mountain #2 runs from middle left to middle right (partially obscured at center by Red Mountain #3 in immediate foreground).

IMOGENE
BASIN

Crystal Lake

Monument Gulch

IRONTON PARK

Tailings

Galena Lion
Gulch

Governor
Gulch

Ironton

Brown
Mtn

Commodore
Gulch

HIGHWAY 550

Red
Mtn #1

IDARADO MINE

Red
Mtn #2

Red Mountain Creek

Red
Mtn #3

Gladstone

GOLD KING MINE

Red Mountain
Pass

Prospect Gulch

N

Cement Creek

Ohio
Peak

Storm
Peak

Ohio Gulch

Figure 13.   AVIRIS 1-µm (Group 1) mineral map of Ironton Park and Red Mountain (#1, #2, and #3, at center) region (fig. 2, inset A) showing distributions of minerals associated with the iron oxide family. The ridge in upper left corner displays different mineralogy because it is outside the Silverton caldera.
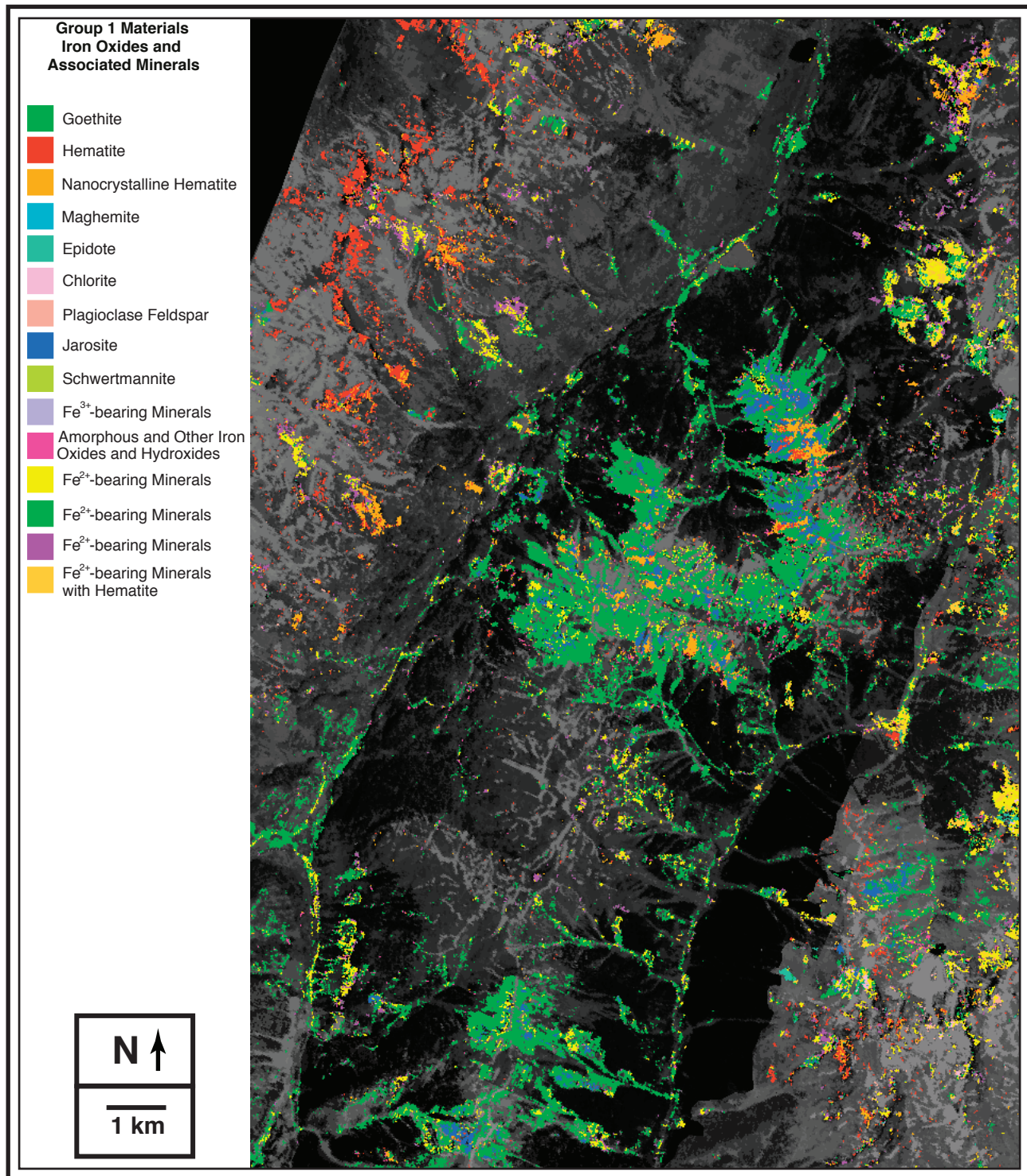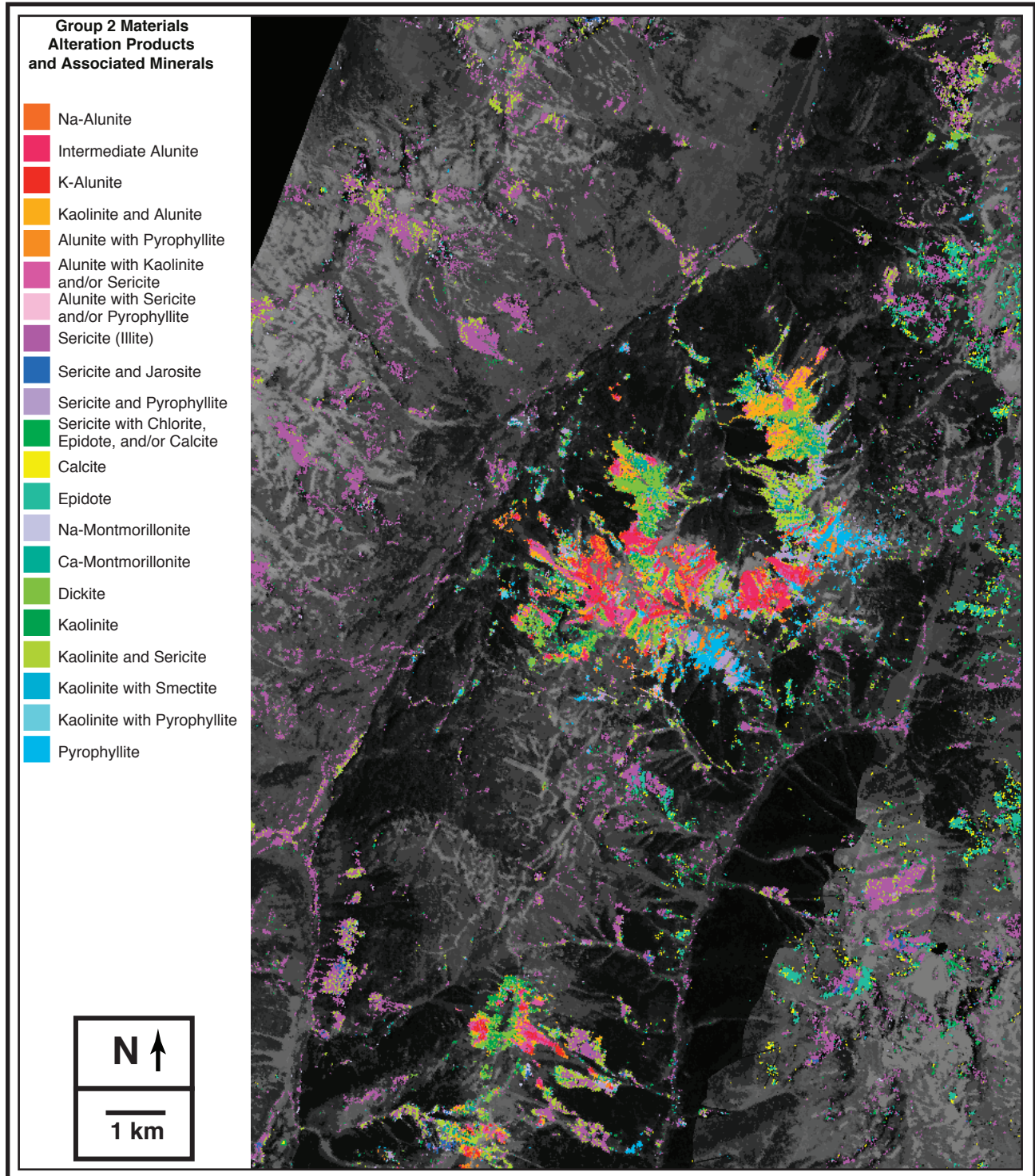
Figure 14. AVIRIS 2-µm (Group 2) mineral map of Ironton Park and Red Mountain (#1, #2, and #3, at center) region (fig. 2, inset A) showing distributions of alteration products and associated minerals, including some mixtures.
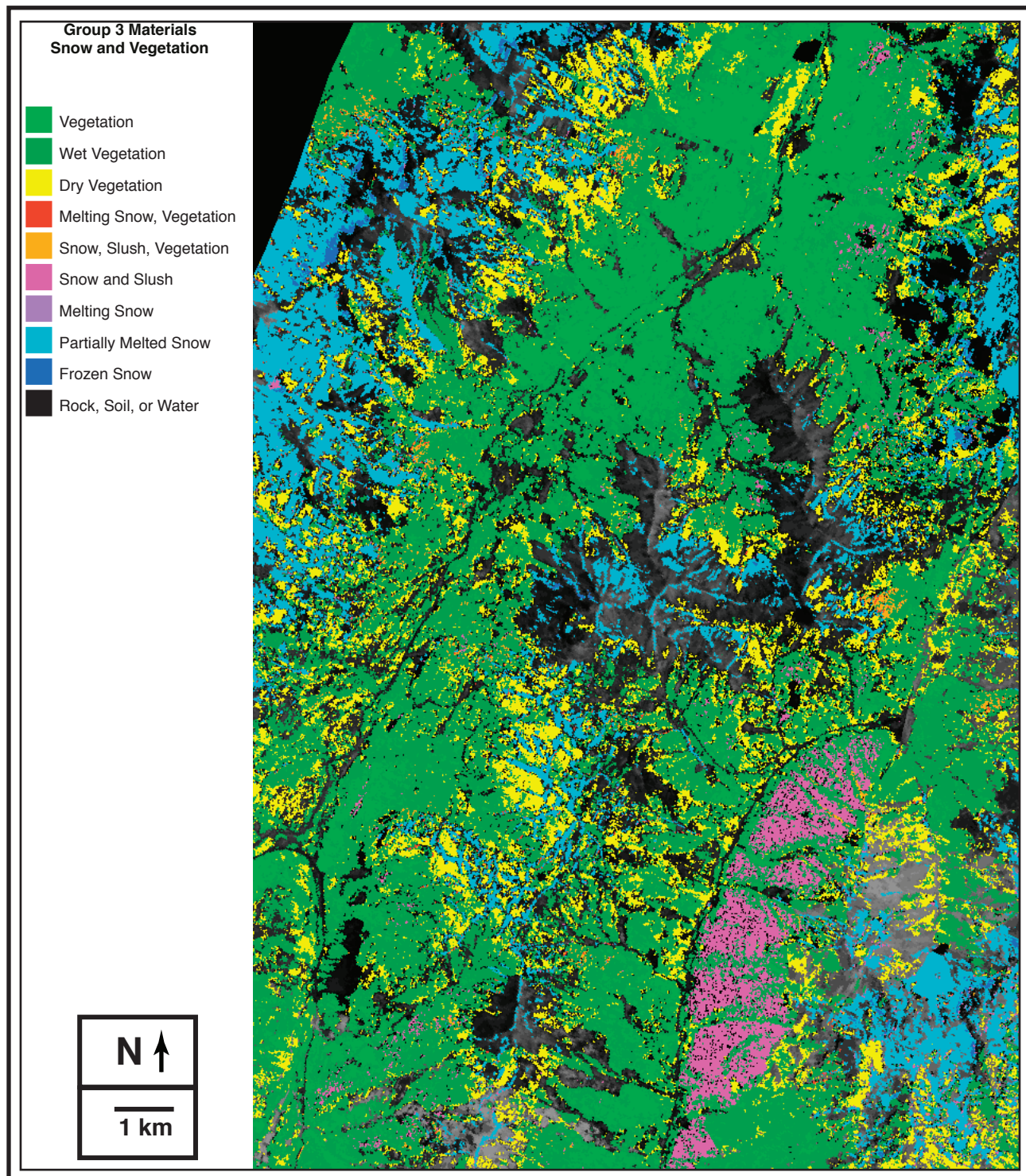
Figure 15.   AVIRIS Group 3 map of Ironton Park and Red Mountain region (fig. 2, inset A) showing distribution of snow, soil, and vegetation.

denoting hematite in the Group 1 (iron oxide) explanation of figure 13 are distributed widely along the ridge connecting Telluride Peak and Hayden Mountain (figs. 9 and 10). These ridges are separated from Red Mountain by Ironton Park and Red Mountain Creek. This creek does not flow into the Animas River; rather it flows northward through Ouray and into the Uncompahgre River. Red Mountain in figure 13 is dominated by the shade of green indicative of goethite in the Group 1 explanation, as well as some jarosite (dark blue) and hematite. These minerals are the products of pyrite weathering that generally define the enormous Red Mountain acid-sulfate alteration; the facing peaks of Telluride and Hayden Mountains are outside the zone of strongest alteration and hence display different mineralogy. Kaolinite and alunite (fig. 14) delineate the main centers of the acid-sulfate alteration zones. Almost no vegetation grows within the most intensely mineralized zones (compare figs. 14 and 15). Calcite, sericite, and chlorite indicative of weaker propylitic alteration (fig. 14) are virtually absent on the peaks of the Red Mountains, but are more abundant farther from the central acid-sulfate alteration zone. Exposures of calcite, epidote, and chlorite begin to predominate near Cement Creek, in the lower right corner of figure 14. As described previously, the ridge to the west also contains abundant propylitic alteration products.

Although the photographs in figures 9, 10, and 11 were taken in midsummer, at the end of July 1997, remnant snow pack from the previous winter abounds. The AVIRIS image cubes were acquired in June 1996, and it is therefore not surprising that they exhibit even more extensive snow cover. This obscures some of the mineralogy, particularly near the mountain peaks. Because snow undergoes changes in grain size as it melts (and refreezes), and because the spectrum of water is different from that of snow, the Tetracorder system finds it simple to differentiate various qualities of the snow pack. Because much of the Animas River watershed is perennially covered by snow and (or) vegetation, it is instructive to view the Tetracorder images for snow and vegetation to see how the mineralogy is obscured.

Figure 15 is a snow and vegetation map for the Ironton and Red Mountain scene. The most heavily mineralized zones, such as the Red Mountains, are typically free of vegetation. Only relatively small areas are completely free of either snow or vegetation. The "wet vegetation" class is widely distributed: the images were acquired in the morning, so dew may account for much of the observed signal. Rainwater is not expected to be a factor, as the sky was clear at the time; however, some standing water may still be on the ground beneath the canopy from a previous rain. Most of the mountain peaks in the image are at least partially covered by frozen snow. Melting snow occurs at the edges of the snow pack, sometimes in combination with vegetation. Snow and slush are readily identified by the spectral combination of liquid water and snow. An interesting phenomenon is apparent in figure 15 to the east of Cement Creek in the lower right of the image. On the lower reaches of this forested, northwest-facing slope, large areas of heavy snow pack have melted and refrozen several times over the course of the summer, yet resisted melting completely. This large-grained snow and slush mixture is found in many locations in the AVIRIS data, and almost always on steep, forested, north-facing slopes.

Given the extensive vegetation cover, one might expect the AVIRIS mineral maps to be more sparse. However, in that the Tetracorder system computes correlation coefficients for all spectra in the reference library, then makes decisions on the basis of these coefficients, it is capable of assigning high confidence levels to more than one material in a given pixel. Hence, small mineralized zones surrounded by vegetation are still evident in the processed images. Cement Creek, for example, is less than a pixel wide in most places along its length. Precipitated minerals along its banks are generally about a meter to either side of the creek. The creek, and the various mineralized areas such as Ohio Gulch which feed into it, are gray in figure 15 but are colored to reveal the presence of alteration minerals in figures 13 and 14. The precipitates along the banks of Cement and other creeks reveal the extent of acidification of the stream waters. Amorphous iron oxides and various Fe^{2+}- and Fe^{3+}-bearing minerals outline the stream reaches (fig. 13), and their strong VNIR absorption features allow them to be identified even where their spatial extent is limited.

Of particular importance are the distributions of minerals associated with acid-generating and acid-neutralizing chemical reactions. The minerals associated with acidic runoff are combined into Group 4, which is a subset of the Group 1 minerals. Group 4 minerals are just those which have been found to be most closely associated with pyrite weathering and acid generation, and include jarosite, goethite, hematite, and amorphous iron oxides and hydroxides (Swayze, Smith, and Clark, 2000; Swayze, Smith, Clark, Sutley, and others, 2000). The extent and distribution of acid-generating potential are most conveniently viewed in the Group 4 mineral maps (fig. 16), because they contain fewer minerals to distract the eye. Furthermore, the image overlays have been constructed with a higher abundance threshold, so that areas containing small amounts of these minerals are not shown. The distribution of goethite, for example, is somewhat less extensive in figure 16 than in figure 13, because only areas of high concentrations are shown. The widespread outcrops of jarosite on the Red Mountains, and additional jarosite in mill tailing piles on the west side of the mountains (fig. 16, center), indicate the presence of large quantities of pyrite in the area. Runoff from these areas contributes to the acidification of Red Mountain, Cement, and Mineral Creeks. The AVIRIS mineral maps reveal that unmined and intensely altered areas contribute significantly to the acidic runoff. Furthermore, the AVIRIS images indicate very little calcite present in this area to neutralize the acidic runoff, resulting in extremely low pH levels (2–4.5), and high concentrations of dissolved metals in these streams (Schemel and others, 2000).

Complementary to the Group 4 AVIRIS mineral maps showing areas of high acid-generation potential are the Group 5 AVIRIS mineral maps showing areas of acid-neutralizing potential (fig. 17). This is generally associated with the presence of

Figure 16.   AVIRIS Group 4 mineral map of Ironton Park and Red Mountain region (fig. 2, inset A) showing distribution of minerals associated with weathering of pyrite. Jarosite (blue) has been found to be an excellent proxy for pyrite, which has no strong VNIR absorption features of its own.
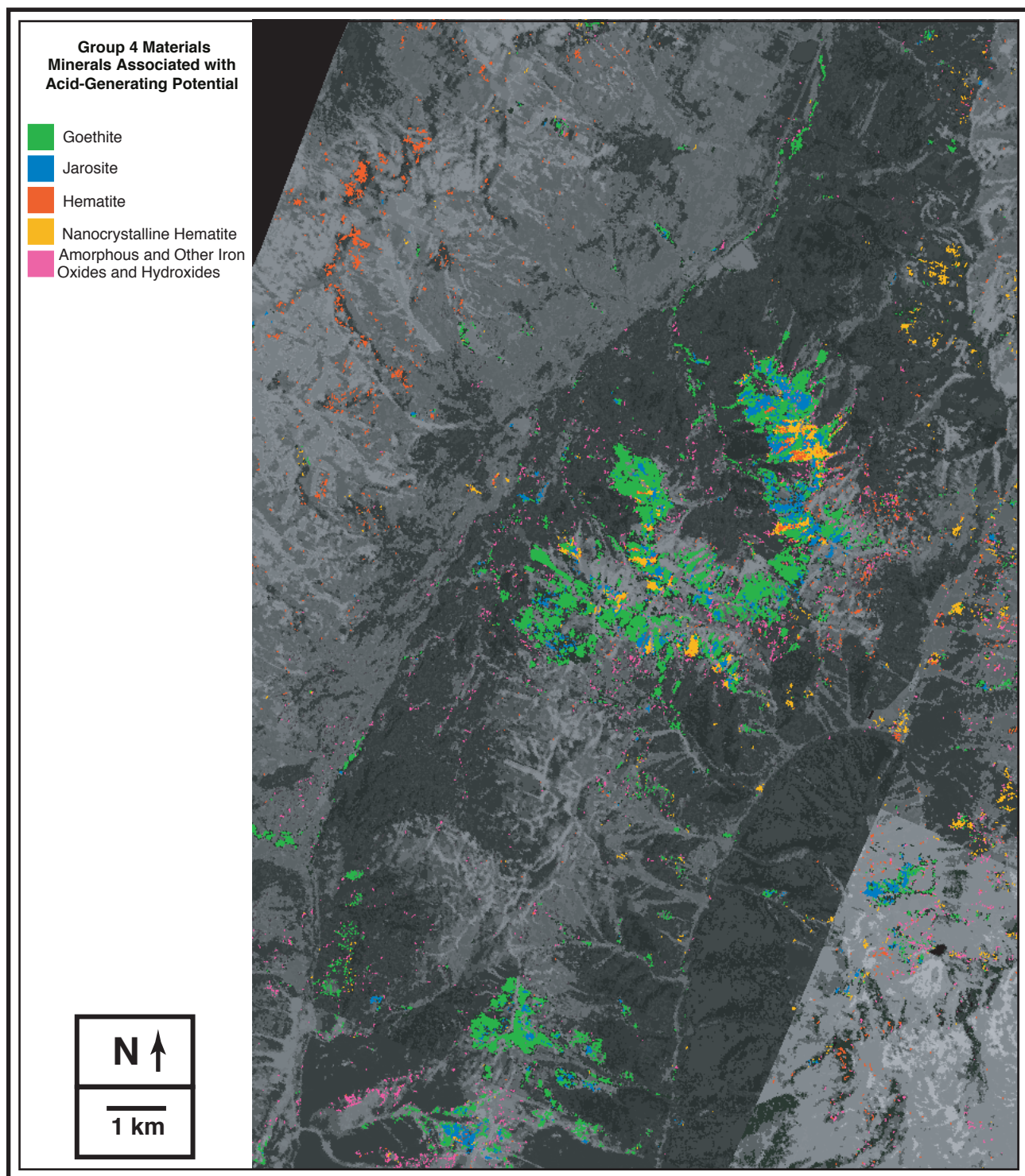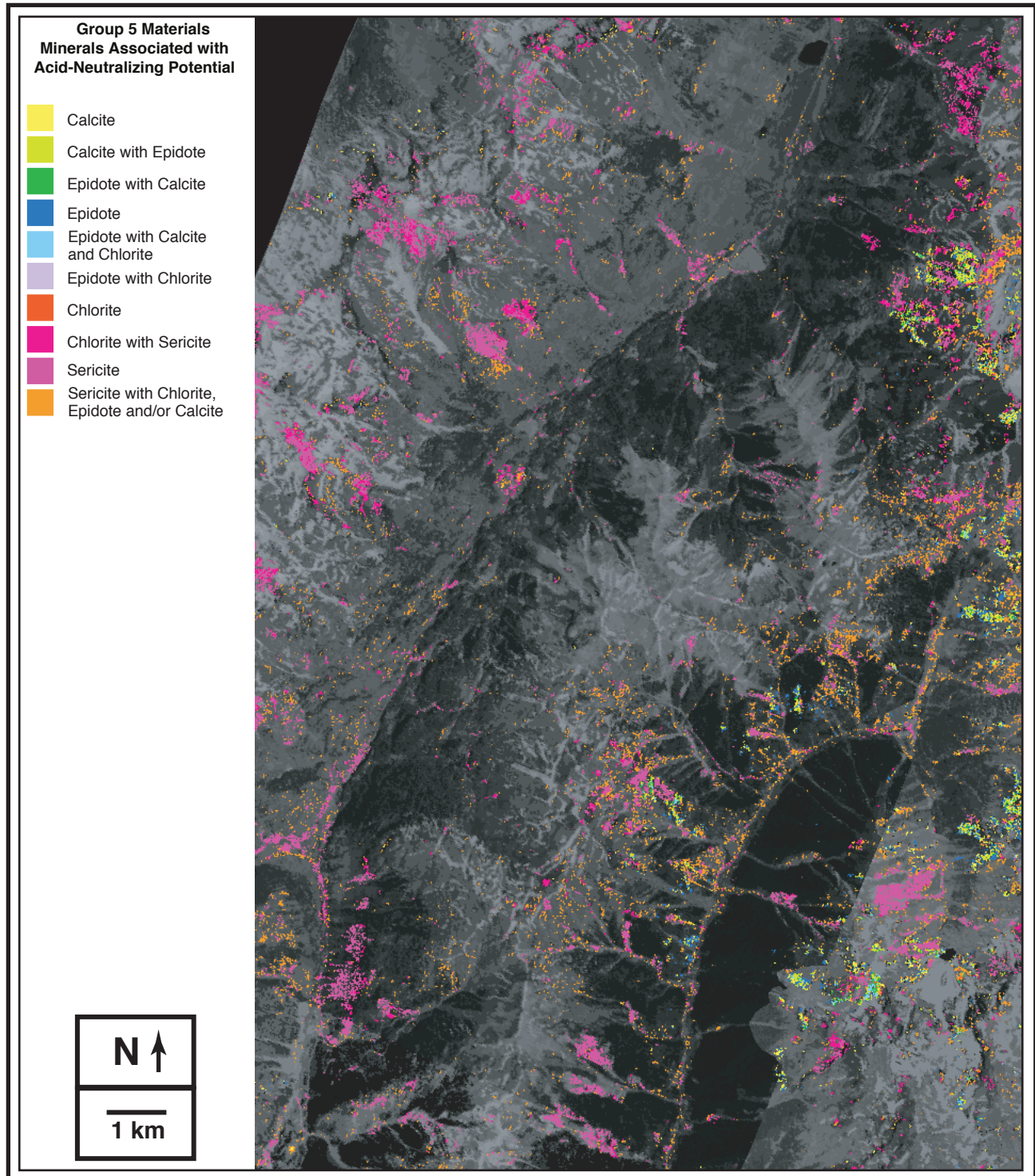
Figure 17. AVIRIS Group 5 mineral map of Ironton Park and Red Mountain region (fig. 2, inset A) showing distribution of calcite, epidote, chlorite, sericite, and mixtures thereof. These distributions have direct relevance to assessments of acid-neutralizing potential.

calcite, and to a lesser extent, chlorite, in propylitic altera- tion zones. The Red Mountains (fig. 16) do not exhibit very much of this mineralogy, but the surrounding areas, particularly to the south and east (fig. 17) have appreciable quantities of calcite, epidote, chlorite, and sericite. These minerals tend to occur together, and so the mixture classes in figure 17 tend to dominate. Several exposures are characterized by variations in relative abundance among these minerals, such as east of Cement Creek and northeast of Brown Mountain (fig. 17).

Animas Forks and the Animas River Upstream from Silverton

The upper Animas River headwaters are located outside of the major areas of most intense hydrothermal alteration. This area (inset B, fig. 2; see also fig. 18) is characterized by a relatively dense network of mineralized veins that are typically accompanied by narrow envelopes of hydrothermally altered rock. However, several large jarosite zones are found, most notably in the vicinity of Houghton, California, Tuttle, Cinnamon, and Eureka Mountains (fig. 19, Group 1). Jarosite zones around the latter three reflect the presence of closely spaced veins and overlapping envelopes of altered rock. In contrast, large zones of jarositic-altered rock in the Houghton and California Mountain areas are indicative of pervasive quartz-sericite-pyrite alteration associated with the intrusion of volatile-rich, high-silica rhyolite plugs. The extent of these exposures appears much larger in the Group 2 mineral map (fig. 20). This is because in the two different images, the jarosite is competing against different mineral spectra for dominance. As discussed previously, the jarosite does not cease to exist at the edges of the dark-blue areas in the image: it is most likely less abundant than the mineral which supersedes it. In the Group 1 mineral map, this is commonly an iron-bearing mineral such as goethite, but in the Group 2 mineral map it is typically sericite. All three minerals may actually coexist. This is a good illustration of how all of the mineral identifications and distributions presented in this study should be interpreted flexibly.

In figure 19, jarosite is associated with the extensive mill tailings along the Animas River near Middleton and Howardsville. In figure 20, however, jarosite is overwhelmed by the spectral signature of sericite at Middleton, and of montmorillonite, an argillic alteration product, at the Howardsville Mill site. This is the only major surface exposure of montmorillonite found in the AVIRIS study and was verified by field-checking and laboratory spectroscopy of hand-collected samples.

The presence of jarosite in the upper Animas River region suggests the potential for significant acidic drainage. Geochemical analyses (Mast and others, 2000), however, indicate that with few exceptions, non-mining related waters are generally of good quality. This is largely because of the absence of large expanses of intensely altered, pyrite-rich rock such as is found in the Red Mountains, Ohio Peak–Anvil

Mountain, and peak 3,792 m areas (Bove and others, 2000; Mast and others, 2000). However, the preponderance of calcite- bearing, propylitic-altered rock in these basins undoubtedly has an acid-neutralizing effect on low-pH runoff where it does occur (Bove and others, 2000; Mast and others, 2000). Appreciable quantities of calcite are evident along the Animas River (fig. 20), most notably around Cataract Gulch, Eureka Mountain, and Burns Gulch, but also elsewhere. This calcite is generally associated with epidote and chlorite. In figure 21, the regions of epidote and calcite from figure 20 are broken down into mixtures of calcite, epidote, chlorite, and sericite, with colors denoting the dominant material(s) in each pixel. The variations in concentration of calcite may be estimated by following the color changes across each area. These variations in composition have been checked in the field by traverses across accessible deposits, such as the 1/4 km exposure paralleling the Animas River just below Cinnamon Mountain. In that pixels contain- ing moderate amounts of calcite are enumerated in addition to those dominated by calcite, the Group 5 mineral assemblage images should prove useful for estimating the potential for acid neutralization occurring along the stream reaches.

Recent laboratory studies (Desborough and others, 1998) indicate that chlorite provides some acid neutralization as well, though on a scale an order of magnitude less than that presented by calcite. Very little chlorite was identified in the Group 1 AVIRIS mineral maps, a notable exception being an area in Hematite Gulch (fig. 19). Although chlorite is rather abundant in the San Juan Mountains, it is spectrally overshadowed in the 1-μm range by other iron-bearing minerals, and in the 2-μm range by sericite. Most of the chlorite detected by this study is in the form of ripidolite (clinochlore group), and its distri- bution is best approximated using the Group 5 images (for example, fig. 21).

Another lesson to be learned from figure 21 is in regards to single-pixel identifications. Large areas of sericite, such as those on the slopes overlooking the South Fork Animas River south of Eureka Gulch (figs. 18 and 21, center) are often surrounded by pixels identified as being dominated by sericite but containing other minerals (orange in fig. 21). Farther out, many scattered small areas meet the criteria for inclusion in this class. In many cases, the spectra of these pixels are contaminated by vegetation, snow cover, and other materials, so that the confidence levels are very close to the minimum threshold values. Such single-pixel units should be interpreted with caution, as noise levels and interference may result in some incorrect identifications.

Silverton and Molas Lake Scenes

As the Animas River flows south past Silverton (inset C, fig. 2; see also fig. 22), pH decreases and significant quantities of metals are added from Cement and Mineral

---

Figure 18 (following page). Geographic features of the upper Animas River region near Animas Forks (fig. 2, inset B).
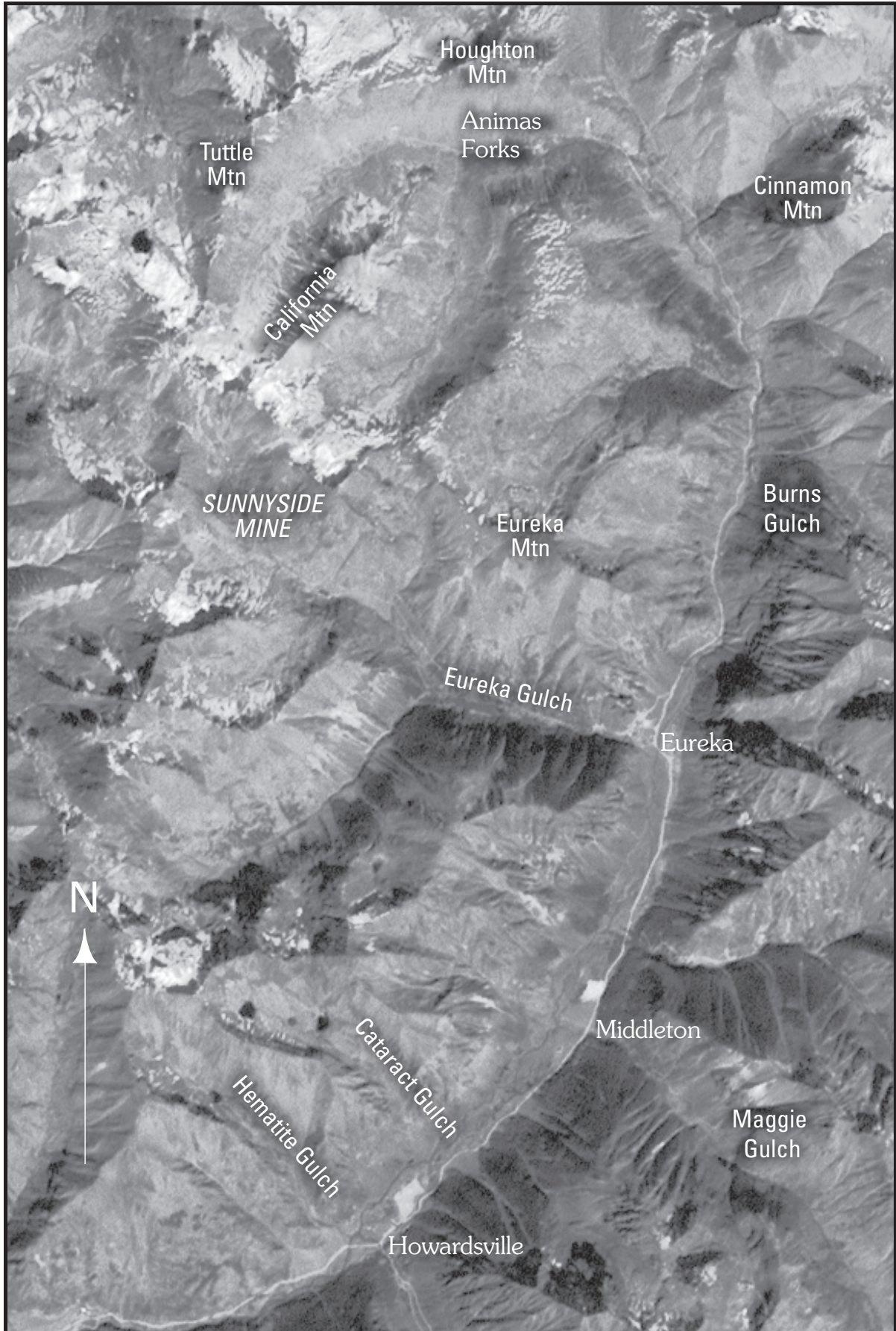
Figure 19.   AVIRIS 1-µm (Group 1) mineral map of upper Animas River near Animas Forks (fig. 2, inset B) showing distributions of iron oxides and associated minerals.

Figure 20. AVIRIS 2-μm (Group 2) mineral map of upper Animas River near Animas Forks (fig. 2, inset B) showing distributions of alteration products and associated minerals.

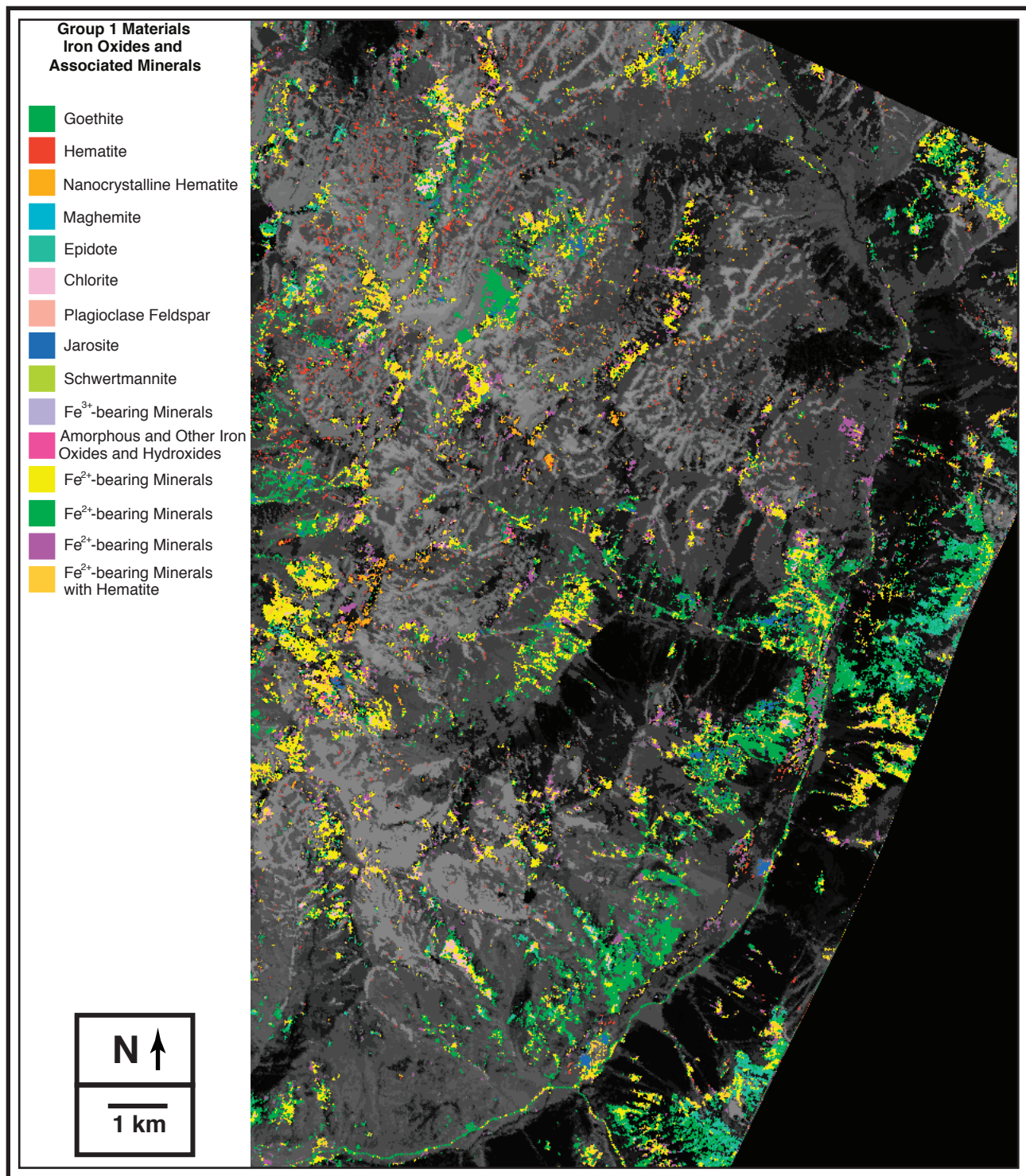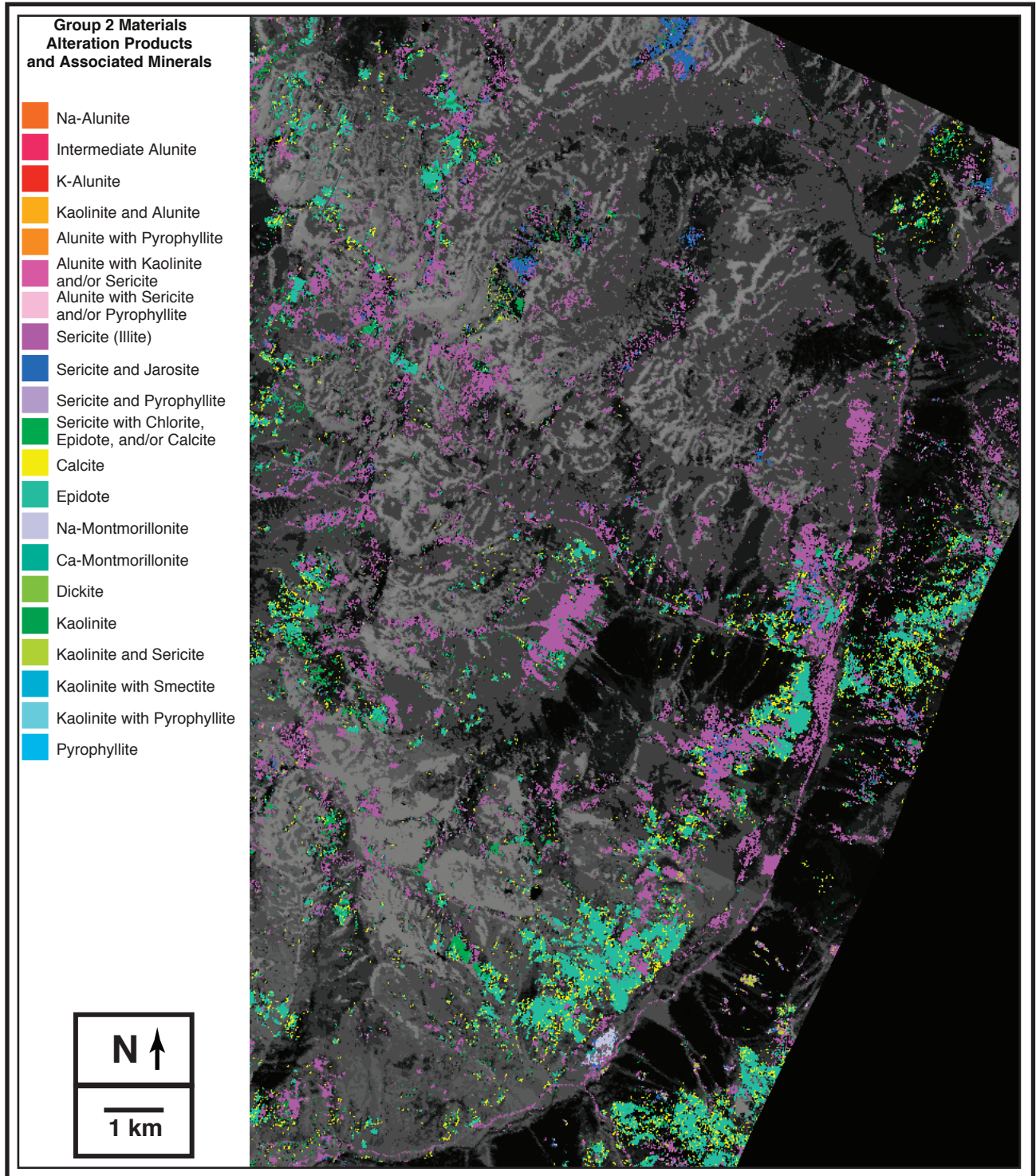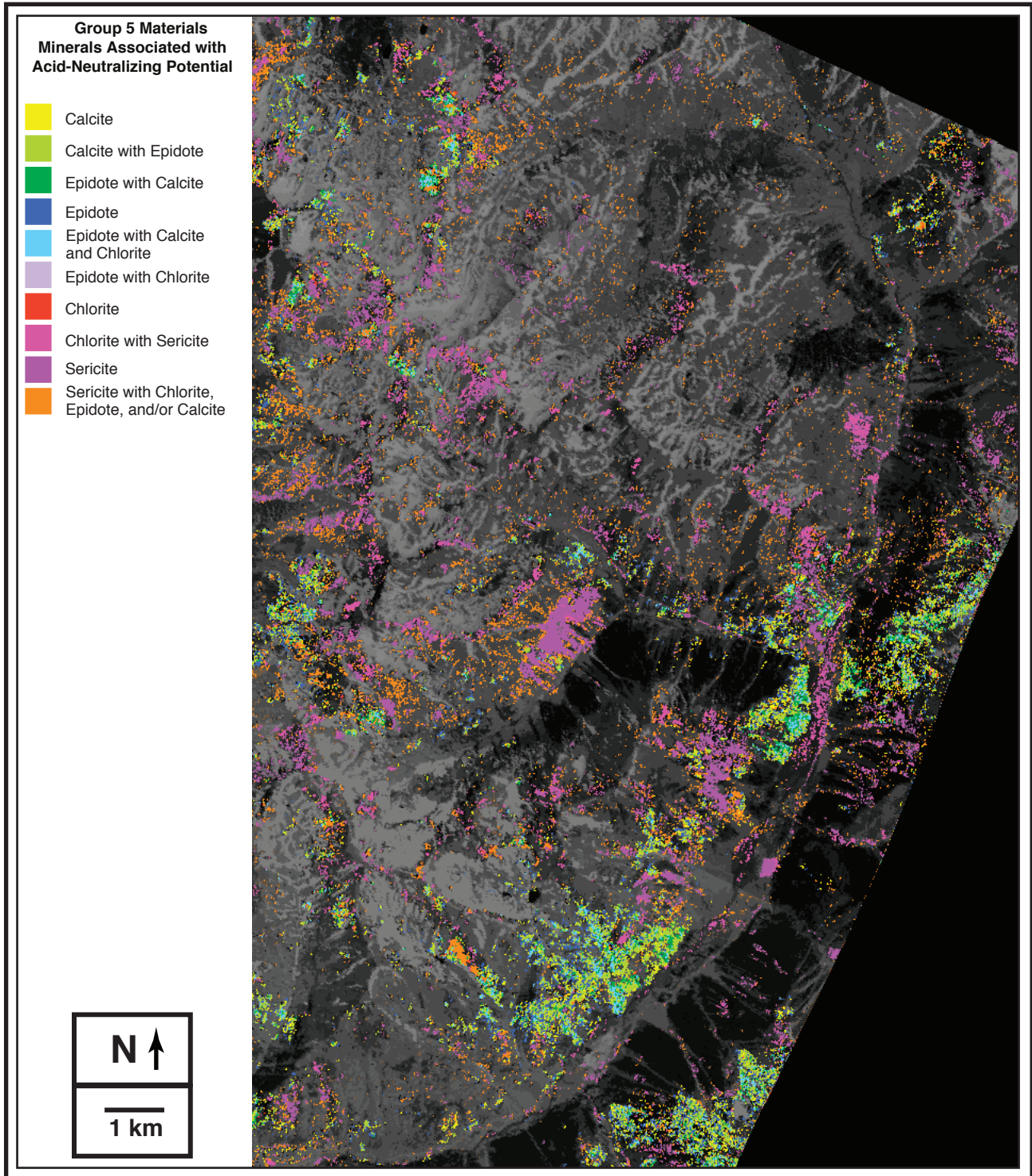**Figure 21.**   AVIRIS Group 5 mineral map of upper Animas River near Animas Forks (fig. 2, inset B) showing distributions of calcite, epidote, chlorite, sericite, and mixtures thereof.

Creeks (Church and others, 1997; Schemel and others, 2000). The town of Silverton is located near the confluences of these two creeks with the Animas River. The streets of the town can be distinguished in the Group 1 AVIRIS mineral map (fig. 23) as a rectangular grid of goethite and other iron-bearing minerals in the roadbeds and gravel, and as sericite in the Group 2 AVIRIS mineral map (fig. 24). The stream beds of Mineral and Cement Creeks, as they cut across the town, are also dominated by goethite and iron-bearing minerals, including amorphous iron oxides and hydroxides precipitated from the streams. As the relatively acidic and metal-laden streams mix with the higher pH waters of the Animas River, aluminum oxy-sulfates and iron oxyhydroxides precipitate, coating the rocks on the banks and in the riverbed (Church and others, 1997). Several areas of oxidized and highly pyritic rock are exposed on the mountainsides overlooking Mineral Creek. As shown in figure 24, these exposures contain alunite and kaolinite. These assignments were field-checked in 1996.

The border between the two AVIRIS flightlines crosses Sultan Mountain southwest of Silverton. This is most obvious as a change in contrast levels in the mosaicked AVIRIS mineral maps (figs. 23, 24). Less apparent effects of the orientation of the AVIRIS platform are illustrated by changes in mineral identifications across the flightline boundary. As viewing angle is different in each flightline, the signal level can differ greatly, especially on steep slopes such as those near the peak of Sultan Mountain. Because many minerals are typically present, different materials may produce a better spectral match on each side of the boundary. This gives rise to such artifacts as the abrupt border of the epidote-dominated region where the flightline crosses Sultan Mountain: in the east part of the image, the epidote signal was below the detection threshold.

Highly altered mineralized areas northwest of Silverton (top center, fig. 24) containing abundant alunite, kaolinite, and pyrophyllite contrast markedly with the less altered mineralogy on either side of the Animas River south of Silverton. Kendall Mountain, Sultan Mountain, and Whitehead Gulch all exhibit the distinct characteristics of propylitic alteration, indicating that they lie outside the central alteration zones of the caldera. The oxidized rocks south of Sultan Mountain are dominated by hematite, which is quite noticeable in figure 23, but they have very little in the way of alteration products with spectral signatures in the 2-μm range (fig. 24).

South of Silverton, the Animas River passes exposures of abundant calcite and epidote on the slopes of Kendall Mountain (fig. 24) and along the riverbed. Eventually it departs the caldera and flows through a sequence of sedimentary rocks containing abundant limestones. The detailed breakdown of acid-neutralizing minerals in figure 25 shows the variation of calcite, epidote, and chlorite concentrations in the propylitic zones on the periphery of the

Silverton caldera. The utility of building a separate image for Group 5 minerals (calcite-epidote-chlorite) is demonstrated by comparison of figures 24 and 25: the acid-neutralizing potential of the rocks just downstream of Silverton in the Animas River canyon is obvious in figure 25 but takes more effort to observe in the much busier Group 2 AVIRIS mineral map (fig. 24). Figure 24 includes a large component of alteration products, north of Mineral Creek, and there are just not enough colors available to visually segregate these materials from the acid-neutralizing assemblages.

Looking farther downstream, sets of parallel yellow bands in the lower left corner of figures 24 and 25 delineate sedimentary limestone beds of the Pennsylvanian-age Hermosa Formation (Yager and Bove, 2002) west of the Animas River near Molas and Andrews Lakes (fig. 22). This much more concentrated form of calcite contributes significant acid-neutralizing potential to the watershed (Church and others, 1997; Desborough and others, 1998). Field investigation of these limestone beds revealed that whereas the yellow banded areas corresponding to calcite identification are confined to a small area, the entire region exhibiting banded structure is also heavily interbedded with limestone. The reason that not all of these bands were recognized by the Tetracorder system is that abundant grasses growing along the rocks obscure the spectral signature.

Engineer Mountain and Purgatory Scenes

Downstream of Silverton the mineralogy of the Animas River watershed becomes much more subdued. South of Molas Lake are some oxidized outcrops containing jarosite and goethite on Snowdon and Twilight Peaks (below C and right of D, fig. 2; see also fig. 1), but there is little hydrothermal alteration evident elsewhere. The Engineer Mountain area (fig. 2, inset D; see also fig. 26) contains abundant vegetation and little in the way of intensely altered rocks. Significant acid-neutralizing potential is contributed to the Animas River by drainage from Lime Creek (fig. 26 and also very visible on east side of area of fig. 27) (Desborough and others, 1998; Mast and others, 2000). Most of this portion of the study area is heavily vegetated, which reduces the amount of surface mineralogy visible to the AVIRIS sensor.

Hematite was identified on Engineer Mountain (fig. 27) from a very faint absorption feature in the 1-μm range. The lightly hematitic talus slopes on the southeast face of Engineer Mountain include the calibration site used for ground-truthing the AVIRIS cubes. The absorption profile of the nanocrystalline hematite on the talus slopes of Engineer

Figure 22 (following page).   Silverton and Molas Lake region of study area (fig. 2, inset C) detailing major geographic features discussed in text.
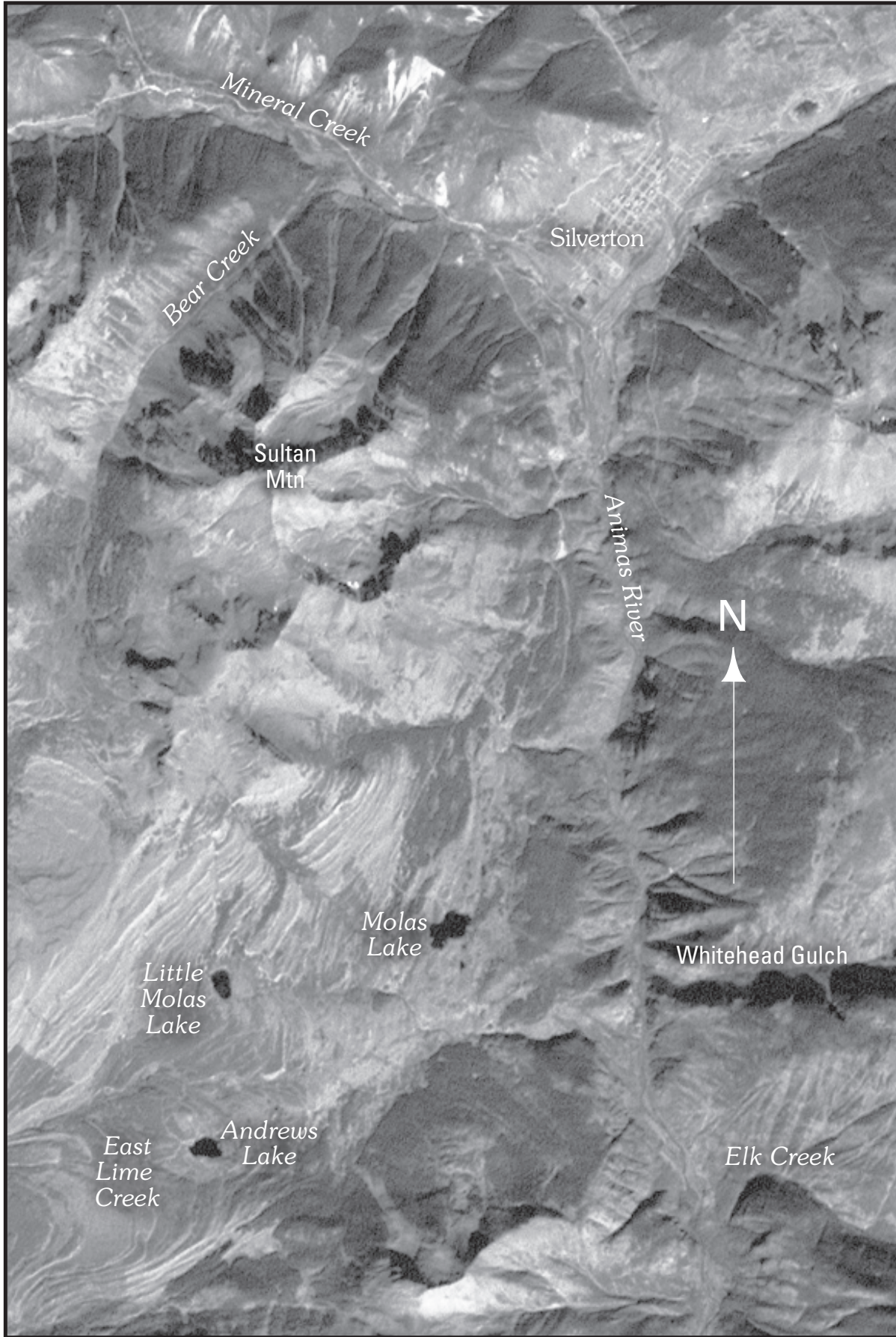
Peak is quite subtle, but the color-coded images produced for this study do not reflect this: the same intensity of color (orange in this case) is used wherever a mineral (hematite in this case) has been identified. Some hematite is evident also at Potato Hill on the right side of the figure, and in the roads and ski trails of the Purgatory Resort (lower left). A number of other iron-bearing minerals were identified in the tributaries of Lime Creek (far right).

Interestingly, the snow and vegetation image (fig. 28) reveals some large-grained slushy snow at lower elevations, such as at Potato Hill. These patches are almost exclusively on steep, north-facing wooded hillsides. This is the same spectral signature of snow beneath a forest canopy identified in figure 15. Frozen and partially melted snow is prevalent only at the peak of Engineer Mountain but can also be discerned in ridged areas near the top (fig. 28). As the elevation has decreased from the headwaters regions, the abundances of snow and various vegetation species have changed significantly. Less snow remains even near the peaks, although wet vegetation occupies a zone about the margin of the peak regions. Wet vegetation is also visible along Cascade and Lime Creeks.

Hermosa and Haviland Lake Scenes

As with the previous scene, most of the lower reaches of the study area (inset E, fig. 2; see also fig. 29) are heavily vegetated, with only limited amounts of exposed rock and soil. Some mineralogy is evident in the Group 1 (fig. 30) image, along the Hermosa Cliffs and on Spud Hill (fig. 29), and in the flats along the Animas River near Stratton Lake and in the southern part of the image area. A few locations along the shores of Haviland and Shalona Lakes also exhibit evidence of iron oxide mineralogy. A selection effect is at work here, as the minerals of greatest interest to this study are abundant in the Silverton caldera and other parts of the northern portion of the study area; and these are the minerals the Tetracorder system was programmed to identify. Hematite is the most widely visible mineral in this image, although there are several others, including calcite, in the mosaics. Hematitic soils, such as in the diamond-shaped field at lower right and nearby residential areas, are classed as hematite in these images. Along the Animas River, a few small areas containing plagioclase feldspar were identified by the mapping algorithm. Subsequent investigation found that these pixels corresponded to rock piles in a commercial gravel operation. Permission was obtained to sample the rock piles, which turned out to be feldspathic river cobbles. Although plagioclase was only identified in small patches throughout the rest of the study region, it was kept in the final images for future reference.

The snow and vegetation image (fig. 31) is typical of the southern reaches of the study area, with only sporadic areas having sufficient exposed mineralogy to be mapped by the Tetracorder system. No significant contributions to acidic runoff are to be expected in this area. Again as with the previous scene (fig. 28), some patches of snow and slush are identified on north-facing steep slopes. Some of these, being single pixels, are suspect and may be there because of subpixel combinations of liquid water and vegetation.

It is worth noting that much of the exposed mineral area apparent in the Hermosa scene (fig. 30) occurs in the original flood plain of the Animas River. Deposition of materials from the upper Animas River is to be expected in this area. High erosion rates and significant human presence, however, have likely obscured any evidence for premining sediment baselines in the area.

Overview and Discussion

The merged AVIRIS flightline mosaics contain a great deal of useful information about the mineralogy of the Animas River watershed study area of this report (area of data acquisition in fig. 2, particularly areas A–E). The hydrothermal alteration zones of the Silverton caldera are easily distinguished on the basis of the primary mineral groups shown in the AVIRIS mineral maps. Minerals associated with acid generation and neutralization of acidic waters can be traced and mapped as they occur throughout the watershed. The general character of the region as viewed by AVIRIS and presented in the mosaics and figure 2 should be more easily interpreted utilizing the descriptions presented in the preceding sections, which provide fundamental background for use of the image mosaics. Detailed investigation of specific areas will be facilitated by an understanding of the limitations inherent to the data and processing methods.

Large, unmined exposures of highly pyritic rock are indicated by the presence of abundant jarosite as observed at peak 3,792 m, Bear Mountain, Animas Forks, Eureka, and the Red Mountains areas. Smaller outcrops are abundant throughout the headwaters areas of the upper Animas River, Cement Creek, and Mineral Creek. The results of this study are useful for identification of areas where both natural and anthropogenic low-pH and metal-bearing water may be present. The lack of large pervasively altered and pyritized zones, and the abundance of acid-neutralizing minerals (calcite and chlorite) within broad expanses of propylitically altered rock along the upper Animas River near Animas Forks, Eureka, and Silverton, likely account for the improved water quality in these areas. Calcite and chlorite are far less prevalent in the Mineral Creek and Cement Creek areas, where stream acidity levels are the highest in the watershed (Church and others, 1997). The interactions of these mineral assemblages explain why the upper Animas River, which drains a basin containing abundant propylitic-altered rocks, has a near-neutral pH (>6.5), while Mineral and Cement Creeks have pH values as low as 4.5.

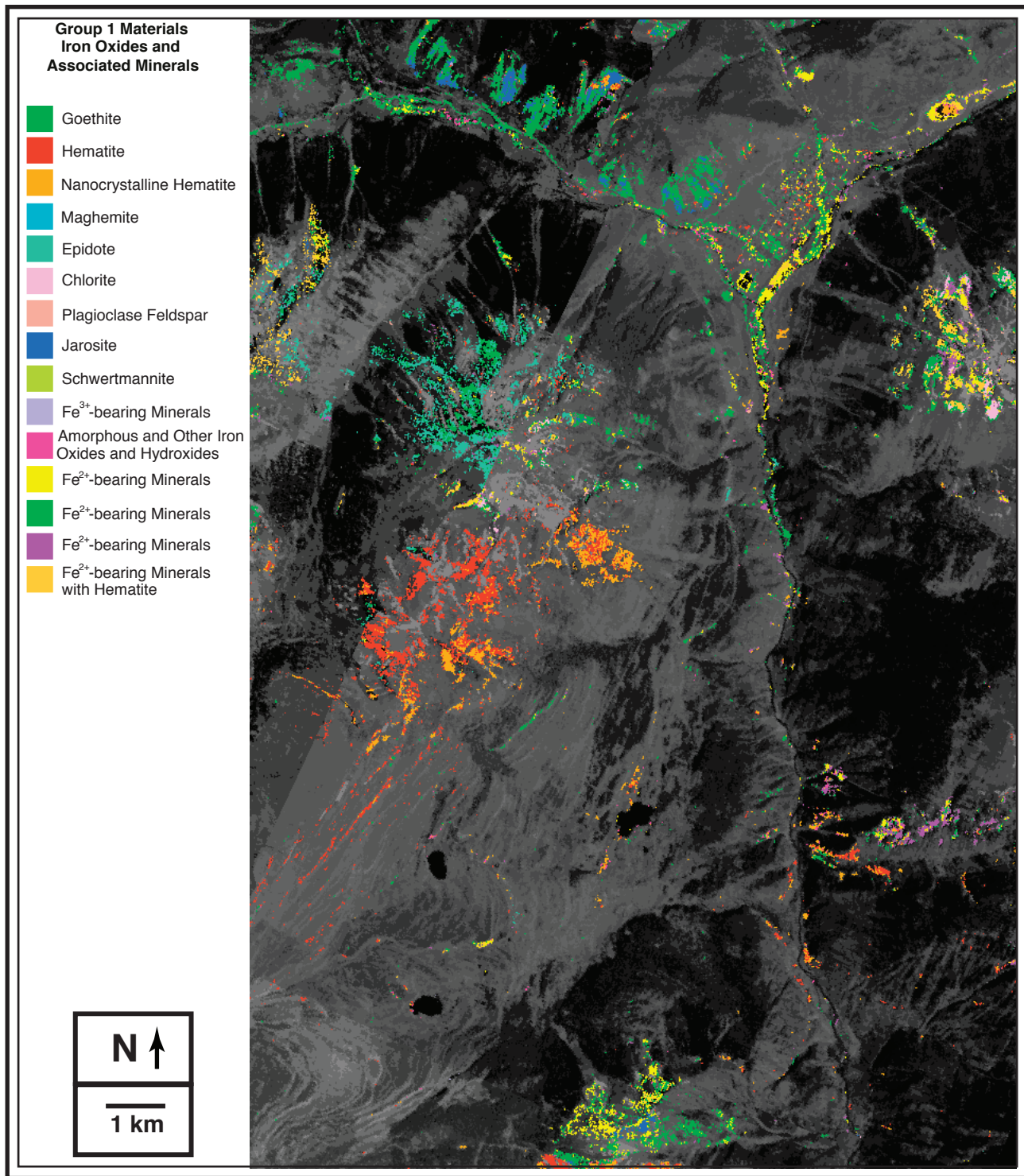**Figure 23.**   AVIRIS 1-μm (Group 1) mineral map of Silverton area (fig. 2, inset C) including Molas Lake. Streets of Silverton stand out in upper right of this image.

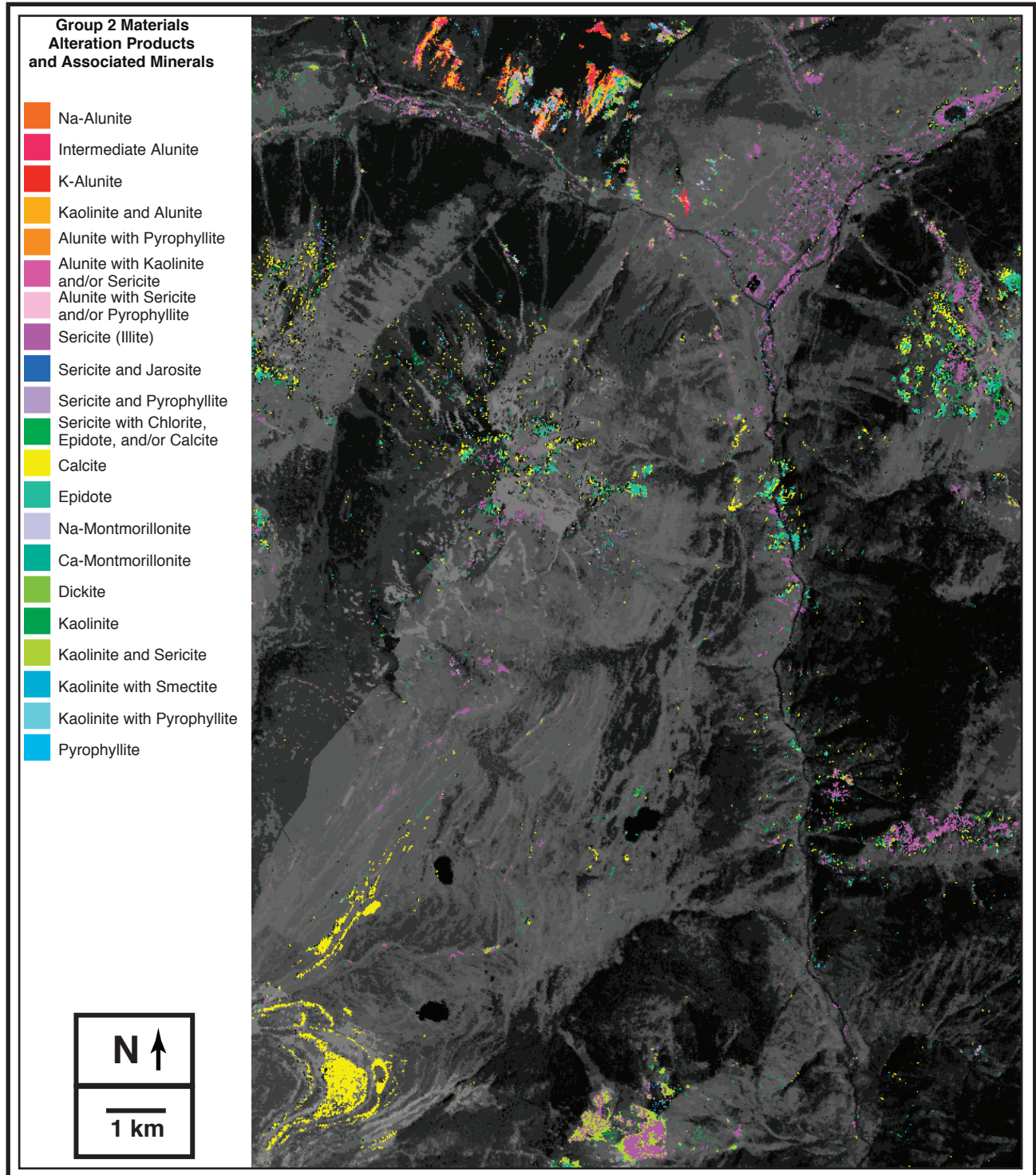**Figure 24.** AVIRIS 2-µm (Group 2) mineral map of Silverton area (fig. 2, inset C) including Molas Lake. Streets of Silverton in upper right appear to be dominated by sericite, whereas beds of limestone map as calcite at lower left.

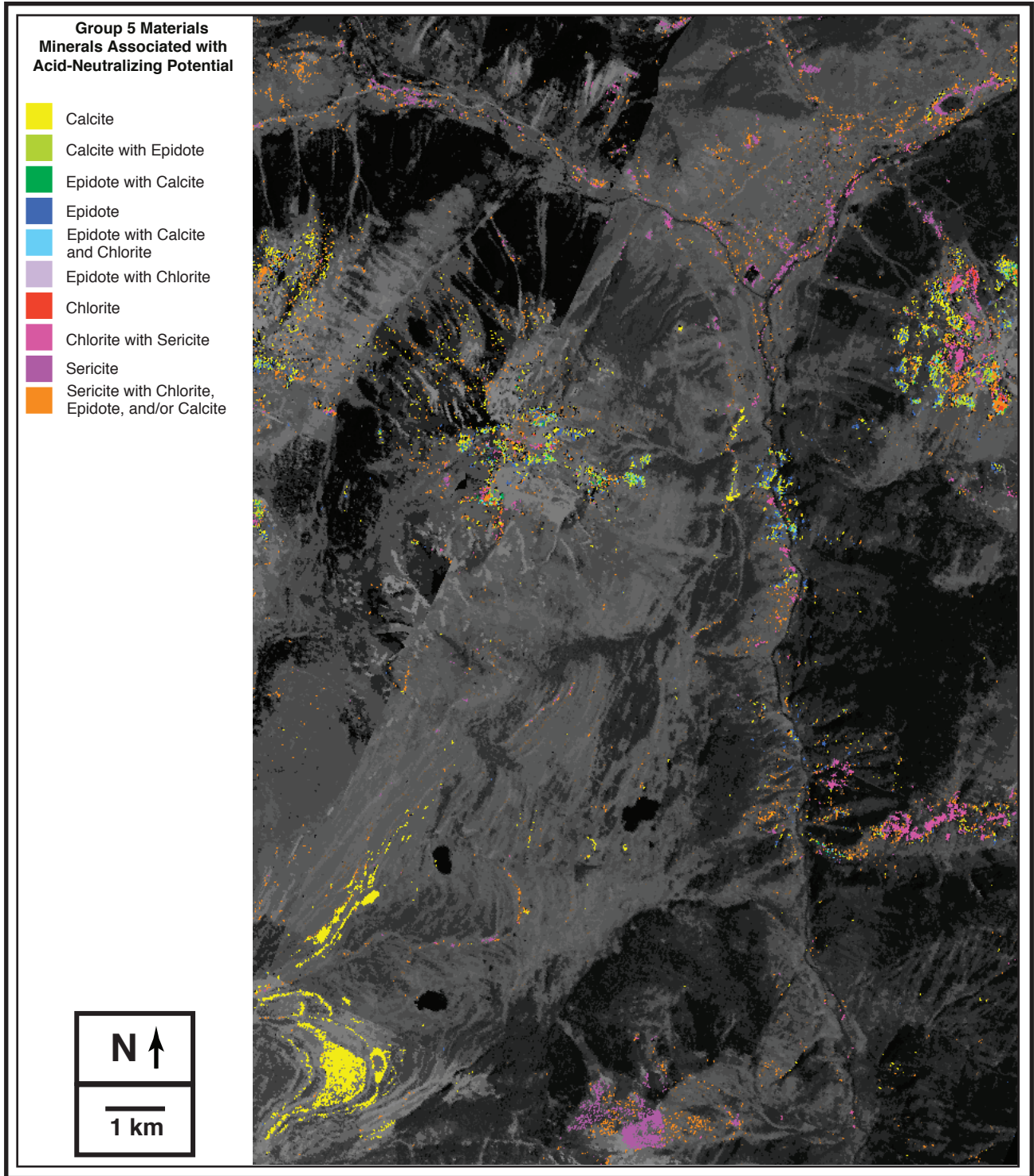**Figure 25.**   AVIRIS Group 5 mineral map of Silverton and Molas Lake area (fig. 2, inset C) showing distributions of calcite, epidote, chlorite, and sericite. The sedimentary limestones at lower left bear much higher concentrations of calcite than are found in zones of propylitic alteration such as those at Sultan Mountain (southwest of Silverton) and Kendall Mountain (upper right, southeast of Silverton).

Determination of the importance and extent of acid-neutralizing minerals should be assisted by the availability of the AVIRIS calcite-epidote-chlorite-sericite (Group 5) mineral maps in this report.

On three separate occasions, fieldwork was performed to verify the accuracy of the Tetracorder results. Although many areas could not be field-verified, spot-checks were made at several locations for every material presented in this report and in the AVIRIS mineral maps. The Tetracorder algorithm was trained and reapplied to the data set until the results matched the field determinations. Additional fieldwork and further refinements to the algorithm and spectral library will most likely result in modification of the specific details of the image mosaics, particularly along the periphery of some mineral zones, and within the calcite-epidote-chlorite-sericite deposits; but the general assessments and distributions are to first order more than sufficient for present purposes.

A great deal of information contained in the AVIRIS data set has not made its way into this report. Specific details of vegetation species, for example, may be extracted using the Tetracorder approach, but this is not of immediate relevance to the present investigation. Certain minerals have been found only in limited regions of the study area, for example schwertmannite, which was found only at the periphery of snow banks or water bodies in regions of strong pyrite oxidation. Meaningful subdivisions of known mineral classes (such as high versus low aluminum-content muscovites, or alunites of varying formation temperatures) have not been included. The full Tetracorder results, which involve more than 400 minerals and material classes, could not be included here because of practical space limitations.

This report does attempt to include some information that may be of use to future investigators having other applications. The Group 1 and Group 2 AVIRIS mineral maps, in particular, contain information on the distributions of more than 37 minerals and mixtures. Every effort was made to assure that this information was of the highest possible quality. This knowledge can be applied not only to studies of water quality, but also to studies of riparian habitats, mineral distributions, environmental impact, structural geology, and hydrothermal alteration processes. The details of snow cover and vegetation distribution, and many of the mineral results, may have other uses unforeseen in the preparation of this report. The spectral library, which is an enhancement of that published in Clark, Swayze, Gallagher, and others (1993), is intended for public release. The techniques of imaging spectroscopy utilized by the Tetracorder 3.6a2 system are still under development, and future improvements are expected (Clark and others, 2003).

Conclusions

The AVIRIS mineral maps presented with this report are intended for general use in studies that require knowledge of the distribution of minerals in the Animas River watershed, and in particular how they relate to water quality issues. The mineral maps are composed of processed image mosaics which have been orthorectified, field checked, and formatted for maximum applicability. The Group 1 AVIRIS mineral maps detail the distributions of iron oxides and associated minerals throughout the watershed, from the Silverton caldera and into the lower reaches of the Animas River. The Group 2 AVIRIS mineral maps of alteration products reveal further details about the hydrothermal and other geologic processes that gave rise to the present landscape. The Group 3 AVIRIS maps illustrate the highly vegetated nature of the watershed and provide a rough estimate of vegetation distributions. In addition, they demonstrate a new approach for discrimination of snow in alpine environments from AVIRIS imaging spectroscopy. This has a number of applications beyond the Animas River watershed (Nolin and Dozier, 1993, 2000; Painter and others, 1998). The Group 4 AVIRIS mineral maps were assembled from a subset of the Iron Oxide and Alteration Products groups. Their usefulness is specific to those concerned with acid-generating potential; the omission of other minerals from these images should make it easier to focus upon the materials of interest. The Group 5 AVIRIS mineral maps represent a further separation of the calcite, epidote, chlorite, and sericite distributions, including mixtures of the four. Though quantitative abundances cannot be precisely determined at present, knowledge of the presence, dominance, or absence of a given material at particular locations is integral to characterization of acid-neutralizing potential.

In the hands of a capable user, the techniques presented here can be used to map surface distributions at a fraction of the cost of traditional field studies. In the Animas River watershed study area, AVIRIS imaging spectroscopy makes it possible to discern the relative abundance and distribution of acid-generating and acid-neutralizing minerals across a large and extremely rugged area. The primary acid-generating mineral assemblages of the Silverton caldera, and their acid-neutralizing counterparts, can now be quantified. While not without its caveats, the AVIRIS study should significantly enhance understanding of water quality issues in the Animas River watershed.

This project demonstrates that imaging spectroscopy data sets over rugged terrain can be accurately calibrated, interpreted, registered, and orthorectified to a standard map base. Difficulties

---

Figure 26 (following page). Engineer Mountain portion of study area (fig. 2, inset D) showing geographic features discussed in text.

Engineer Mtn

COAL BANK PASS

Ground Calibration Site

HIGHWAY 550

Lime Creek

Cascade Creek
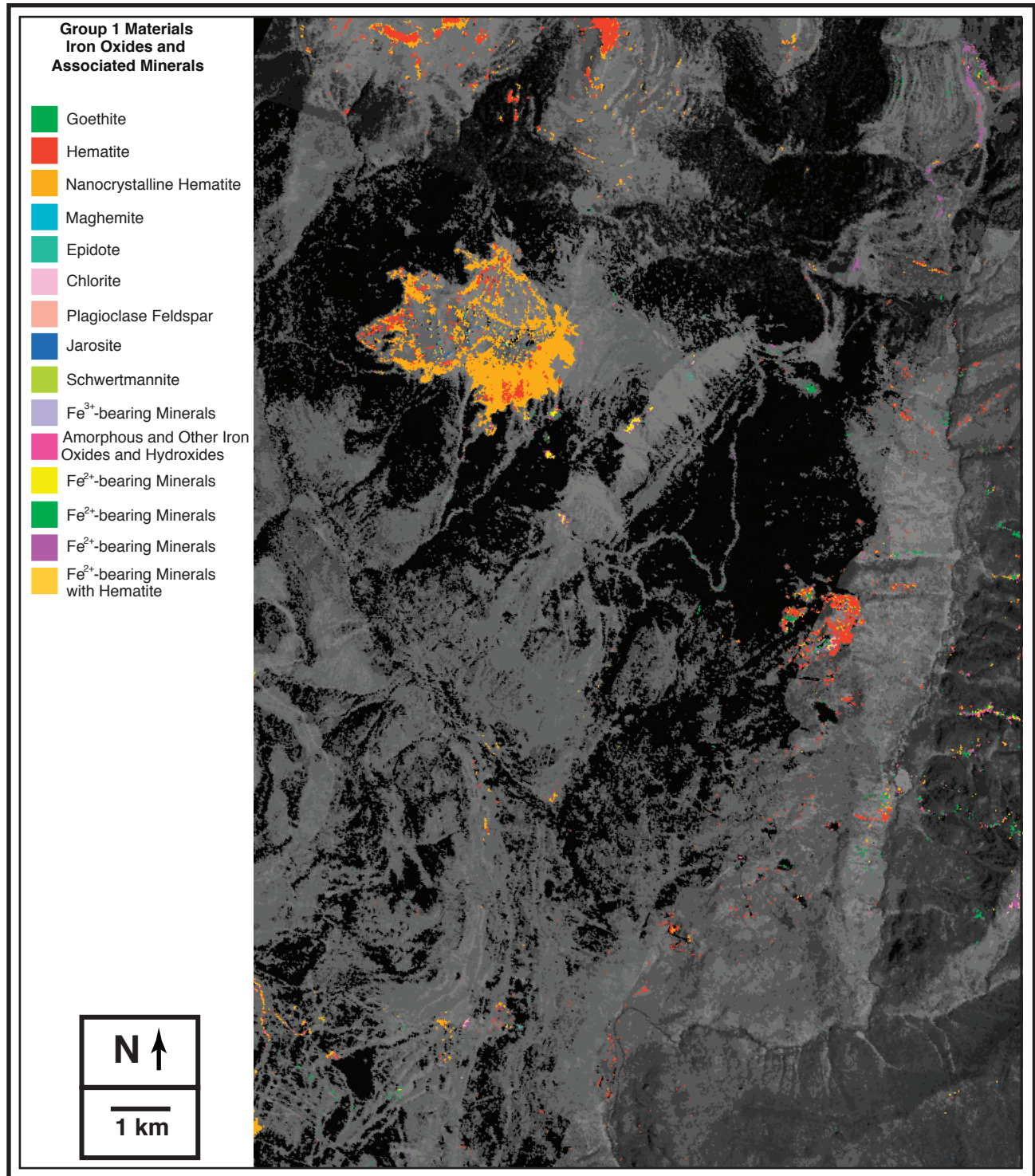
Potato Hill

N

Purgatory Resort

Figure 27.   AVIRIS Group 1 mineral map of Engineer Mountain region (fig. 2, inset D) showing distribution of iron oxides, predominantly hematite. Heavy vegetation in this portion of the study area obscures much of the mineralogy.
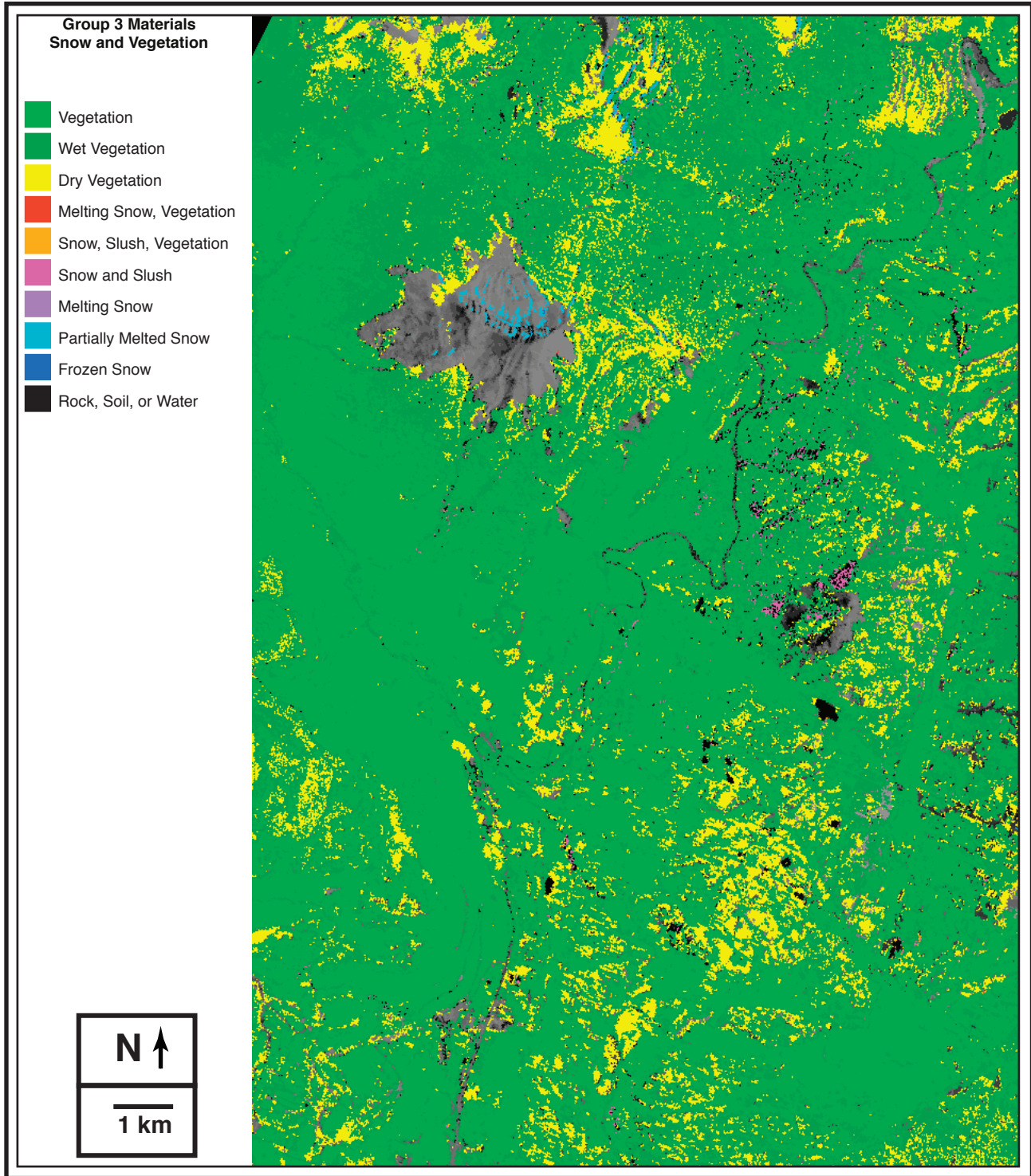
Figure 28.   AVIRIS Group 3 map of Engineer Mountain region (fig. 2, inset D) demonstrating the prevalence of thick vegetation throughout the area. Some snow is also found at high altitudes and on protected north-facing slopes.

Figure 29 (following page).   Hermosa and Haviland Lake region of study area (fig. 2, inset E) showing geographic features discussed in text.
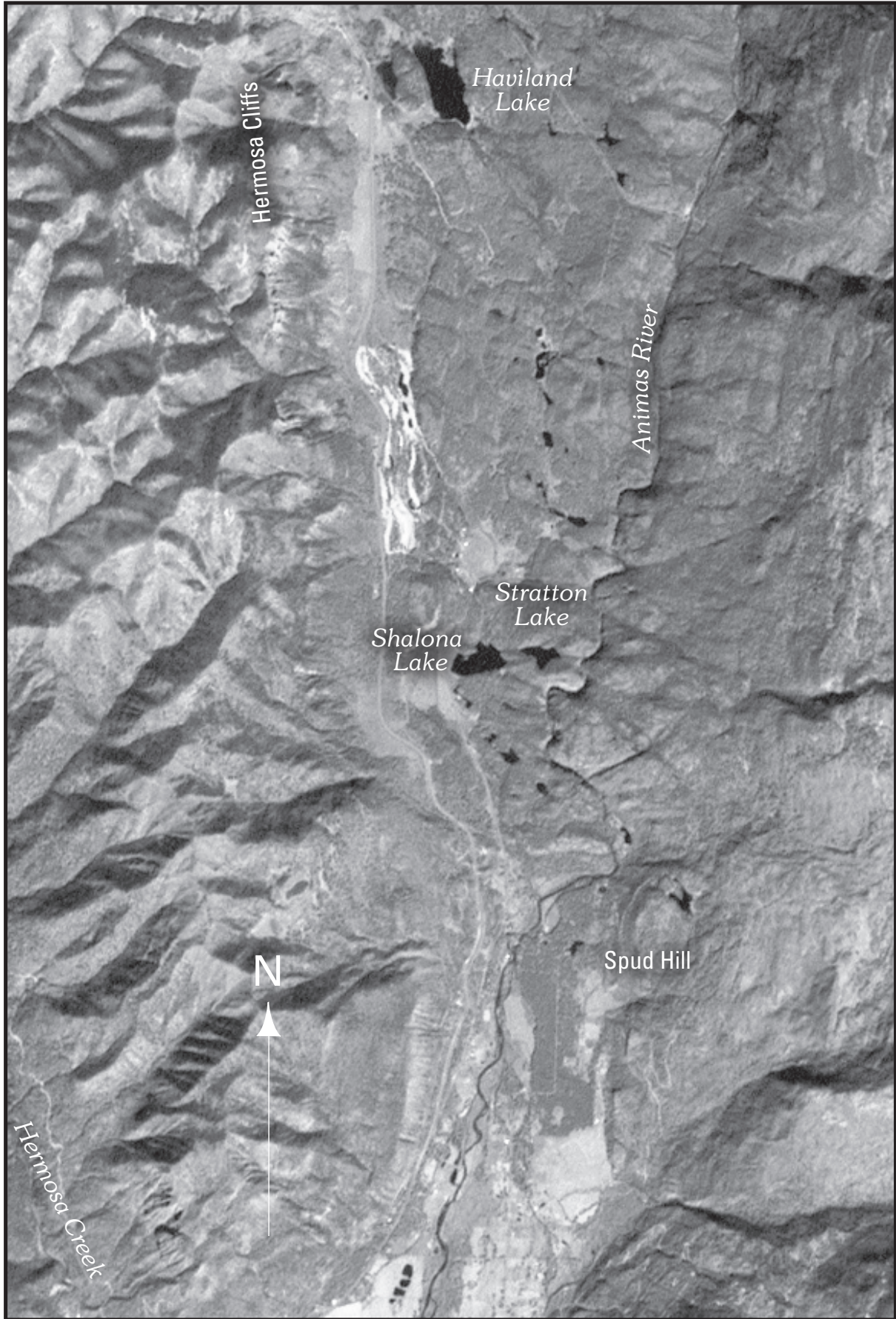
Figure 30.   AVIRIS Group 1 mineral map of Hermosa region (fig. 2, inset E) showing distributions of exposed iron oxides and associated minerals.

Figure 31.   AVIRIS Group 3 map of Hermosa and Haviland Lake region (fig. 2, inset E), detailing snow and vegetation cover.
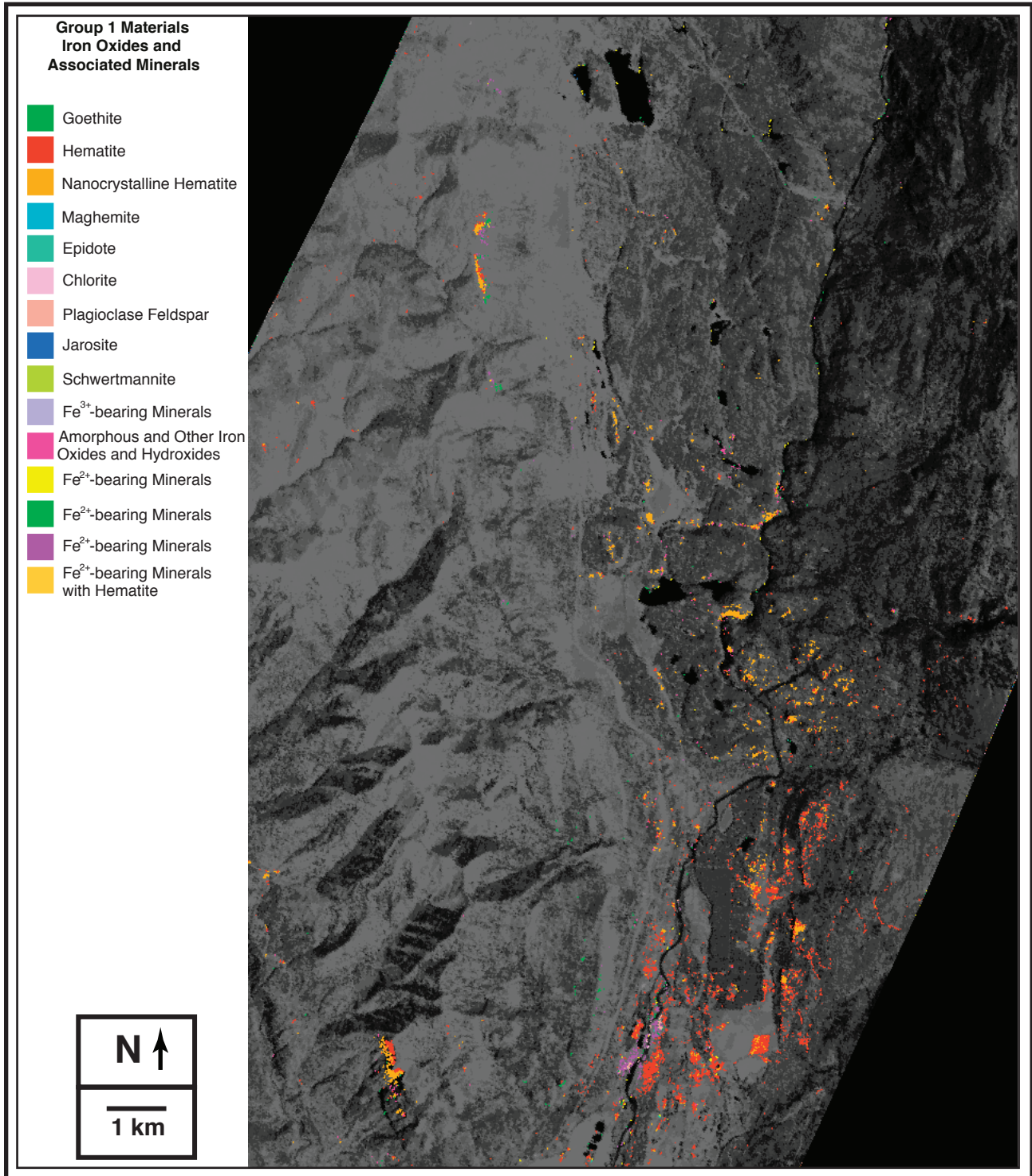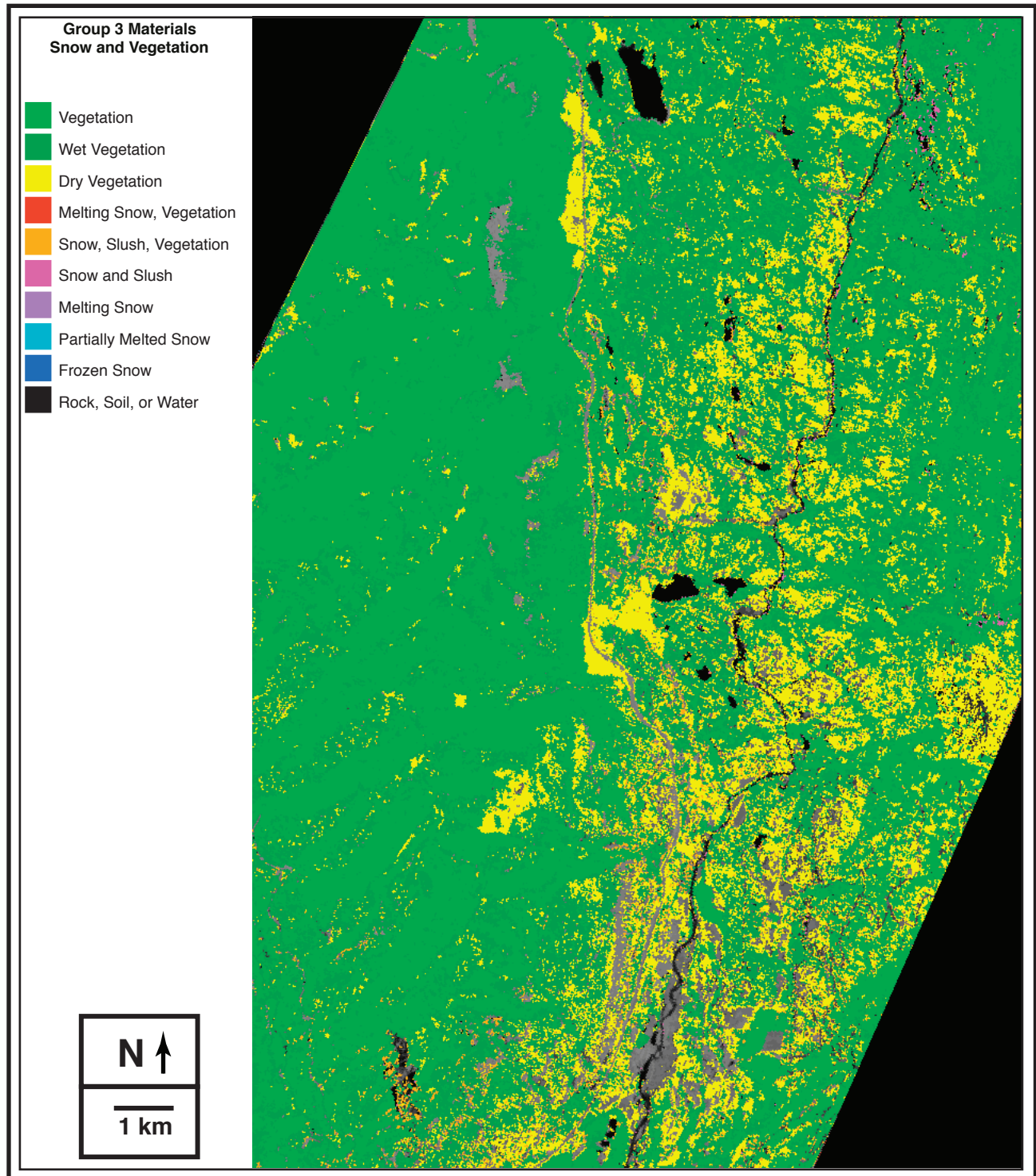
specific to the airborne AVIRIS high-altitude ER-2 platform have been overcome, and those caused by the extreme elevation changes in the San Juan Mountains have been shown to be surmountable. In addition, even materials having their diagnostic spectral absorptions at the same wavelength may be successfully discriminated by the Tetracorder approach. Future improvements to the AVIRIS sensor and Tetracorder expert system should provide even more powerful techniques for remote sensing. The expected advent of orbiting civilian imaging spectrometers will undoubtedly create new directions for geologic investigations.

References Cited

Ashley, R.P., 1974, Goldfield mining district: Nevada Bureau of Mines and Geology Report 19, p. 49–66.

Bevington, P.R., 1992, Data reduction and error analysis for the physical sciences, Second Edition: New York, McGraw-Hill, 328 p.

Bird, A.G., 1999, Silverton gold, the story of Silverton's largest gold mine (revised edition): Lakewood, Colo., privately published, 223 p.

Bookstein, F.L., 1989, Principal warps—Thin-plate splines and the decomposition of deformations: IEEE Transactions on Pattern Analysis and Machine Intelligence, v. 11, no. 6, p. 567–585.

Bove, D.J., Hon, Ken, Budding, K.E., Slack, J.F., Snee, L.W., and Yeoman, R.A., 2001, Geochronology and geology of late Oligocene through Miocene volcanism and mineralization in the western San Juan Mountains, Colorado: U.S. Geological Survey Professional Paper 1642, 30 p.

Bove, D.J., Mast, M.A., Wright, W.G., Meeker, G.P., Yager, D.B., and Verplanck, P.L., 2000, Geologic control on acidic and metal-rich waters in the southeast Red Mountain area, near Silverton, Colorado, *in* ICARD 2000; Proceedings of the Fifth International Conference on Acid Rock Drainage, Volume 1: Society for Mining, Metallurgy, and Exploration, Inc., p. 523–533.

Bove, D.J., Wright, W.G., Mast, M.A., and Yager, D.B., 1998, Natural contributions of acidity and metals to surface waters of the upper Animas River watershed, Colorado, *in* Nimick, D.A., and von Guerard, Paul, eds., Science for watershed decisions on abandoned mine lands; Review of preliminary results: U.S. Geological Survey Open-File Report 98-0297.

Burbank, W.S., and Luedke, R.G., 1969, Geology and ore deposits of the Eureka and adjoining districts, San Juan Mountains, Colorado: U.S. Geological Survey Professional Paper 535, 73 p.

Burns, R., 1993, Mineralogical applications of crystal field theory, Second Edition: Cambridge, Mass., Cambridge University Press, 551 p.

Casadevall, Thomas, and Ohmoto, Hiroshi, 1977, Sunnyside mine, Eureka mining district, San Juan County, Colorado; Geochemistry of gold and base metal ore deposition in a volcanic environment: Economic Geology, v. 92, p. 1285–1320.

Church, S.E., Fey, D.L., and Blair, Robert, 2000, Pre-mining bed sediment geochemical baseline in the Animas River Watershed, southwestern Colorado, *in* ICARD 2000; Proceedings of the Fifth International Conference on Acid Rock Drainage, Volume 1: Society for Mining, Metallurgy, and Exploration, Inc., p. 499–512.

Church, S.E., Kimball, B.A., Fey, D.L., Ferderer, D.A., Yager, T.J., and Vaughn, R.B., 1997, Source, transport, and partitioning of metals between water, colloids, and bed sediments of the Animas River, Colorado: U.S. Geological Survey Open-File Report 97-151, 136 p.

Clark, R.N., 1999, Spectroscopy of rocks and minerals, and principles of spectroscopy, *in* Rencz, A.N., ed., Manual of remote sensing, Third Edition, Volume 3, Remote sensing for the earth sciences: New York, John Wiley, 741 p.

Clark, R.N., Gallagher, A.J., and Swayze, G.A.S., 1990, Material absorption band depth mapping of imaging spectrometer data using a complete band shape least-squares fit with library reference spectra, *in* Proceedings of the 2nd Airborne Visible / Infrared Imaging Spectrometer (AVIRIS) Workshop: Pasadena, Calif., JPL Publication 90-54, Jet Propulsion Laboratory, p. 176–186.

Clark, R.N., Livo, K.E., and Kokaly, R.F., 1998, Geometric correction of AVIRIS imagery using on-board navigation and engineering data, *in* Summaries of the 7th JPL Airborne Earth Science Workshop—Volume 1, AVIRIS Workshop: Pasadena, Calif., JPL Publication 97-21, Jet Propulsion Laboratory, p. 57–65.

Clark, R.N., and Roush, T.L., 1984, Reflectance spectroscopy— Quantitative analysis techniques for remote sensing applications: Journal of Geophysical Research, v. 89, p. 6329–6340.

Clark, R.N., and Swayze, G.A.S., 1995, Mapping minerals, amorphous materials, environmental materials, vegetation, water, ice and snow, and other materials—The USGS Tricorder algorithm, *in* Summaries of the 5th Annual JPL Airborne Earth Science Workshop: Pasadena, Calif., JPL Publication 95-1, Jet Propulsion Laboratory, p. 39–40.

Clark, R.N., Swayze, G.A.S., and Gallagher, A., 1993, Mapping materials with imaging spectroscopy: U.S. Geological Survey Office of Mineral Resources Bulletin 2039, p. 141–150.

Clark, R.N., Swayze, G.A.S., Gallagher, A.J., Gorelick, N., and Kruse, F., 1991, Mapping with imaging spectrometer data using the complete band shape least-squares algorithm simultaneously fit to multiple spectral features from multiple materials, *in* Proceedings of the 3rd Airborne Visible / Infrared Imaging Spectrometer (AVIRIS) Workshop: Pasadena, Calif., JPL Publication 91-28, Jet Propulsion Laboratory, p. 2–3.

Clark, R.N., Swayze, G.A.S., Gallagher, A., King, T.V.V., and Calvin, W.M., 1993, The U.S. Geological Survey Digital Spectral Library; Version 1; 0.2 to 3.0 μm: U.S. Geological Survey Open File Report 93-592, available at URL http://speclab.cr.usgs.gov, 1,340 p.

Clark, R.N., Swayze, G.A.S., Heidebrecht, K.B., Goetz, A.F.H., and Green, R.O., 1993, Comparison of methods for calibrating AVIRIS data to ground reflectance, *in* Summaries of the 4th Annual JPL Airborne Geosciences Workshop—Volume 1, AVIRIS Workshop: Pasadena, Calif., JPL Publication 93-26, Jet Propulsion Laboratory, p. 31–34.

Clark, R.N., Swayze, G.A.S., Livo, K.E., Kokaly, R.F., King, T.V.V., Dalton, J.B., Vance, J.S., Rockwell, B.W., Hoefen, T., and McDougal, R.R., 2002, Surface Reflectance Calibration of Terrestrial Imaging Spectroscopy Data—A tutorial using AVIRIS: Proceedings of the 11th JPL Airborne Earth Science Workshop: Pasadena, Calif., JPL Publication 03-4, Jet Propulsion Laboratory, p. 43–63.

Clark, R.N., Swayze, G.A., Livo, K.E., Kokaly, R.F., Sutley, S.J., Dalton, J.B., McDougal, R.R., and Gent, C.A., 2003, Imaging spectroscopy—Earth and planetary remote sensing with the USGS Tetracorder and expert systems: Journal of Geophysical Research, 108(E12), 5131, doi:10.1029/2002JE001847, p. 5-1 to 5-44 [December 2003].

Dalton, J.B., 2000, Constraints on the surface composition of Jupiter's moon Europa based on laboratory and spacecraft data: Boulder, Colo., University of Colorado Ph. D. dissertation, 253 p.

Dalton, J.B., Bove, D.J., Mladinich, C.S., Clark, R.N., Rockwell, B.W., Swayze, G.A.S., King, T.V.V., and Church, S.E., 2002, Spectral classification of similar materials using the USGS Tetracorder algorithm—The calcite-epidote-chlorite problem, *in* Green, R.O., ed., Summaries of the 10th Annual JPL Airborne Earth Science Workshop: Pasadena, Calif., JPL Publication 02-1, Jet Propulsion Laboratory, p. 93–103.

Dalton, J.B., Bove, D.J., Mladinich, C.S., and Rockwell, Barnaby, 2004, Classification of spectrally similar materials using the Tetracorder algorithm—The calcite-epidote-chlorite problem: Remote Sensing of Environment, v. 89, p. 455–466.

Dalton, J.B., King, T.V.V., Bove, D.J., Kokaly, R.F., Clark, R.N., Vance, J.S., and Swayze, G.A.S., 1998, Mapping of acid-generating and acid-buffering minerals in the Animas watershed by AVIRIS spectroscopy, *in* Green, R.O., ed., Summaries of the 7th Annual JPL Airborne Earth Science Workshop: Pasadena, Calif., JPL Publication 97-21, Jet Propulsion Laboratory, p. 79–83.

Dalton, J.B., King, T.V.V., Bove, D.J., Kokaly, R.F., Clark, R.N., Vance, J.S., and Swayze, G.A.S., 2000, Distribution of acid-generating and acid-buffering minerals in the Animas River watershed by AVIRIS spectroscopy, *in* ICARD 2000; Proceedings of the Fifth International Conference on Acid Rock Drainage, Volume 2: Society for Mining, Metallurgy, and Exploration, Inc., p. 1541–1550.

Desborough, G.A., Briggs, P.H., and Mazza, Nilah, 1998, Chemical and mineralogical characteristics and acid-neutralizing potential of fresh and altered rocks and soils of the Boulder River headwaters in Basin and Cataract Creeks of northern Jefferson County, Montana: U.S. Geological Survey Open File Report 98-40, 21 p.

Eberl, D.D., Srodon, J., Lee, M., Nadeau, P.H., and Northrup, H.R., 1987, Sericite from the Silverton caldera, Colorado—Correlation among structure, composition, origin and particle thickness: American Mineralogist, v. 72, p. 914–934.

Ehlers, M., 1994, Geometric registration of airborne scanner data using multiquadric interpolation techniques, *in* Proceedings of the First International Airborne Remote Sensing Conference and Exhibition, Strasbourg: Ann Arbor, Mich, Environmental Research Institute of Michigan, p. 492–502.

Ehlers, M., and Fogel, D.N., 1994, High-precision geometric correction of airborne remote sensing revisited—The multiquadric interpolation, in Proceedings of the International Society for Optical Engineering Conference; Image and Signal Processing for Remote Sensing, Rome, Italy, Sept. 26-30, 1994: Rome, International Society for Optical Engineering, v. 2315, p. 814–824.

Fisher, F.S., and Leedy, W.P., 1973, Geochemical characteristics of mineralized breccia pipes in the Red Mountain district, San Juan Mountains, Colorado: U.S. Geological Survey Bulletin 1381, 43 p.

Fleischer, Michael, and Mandarino, J.A., 1995, Glossary of mineral species, Seventh Edition: Mineralogical Record, 280 p.

Gao, B.C., Heidebrecht, K.B., and Goetz, A.F.H., 1993, Derivation of scaled surface reflectances from AVIRIS data: Remote Sensing of Environment, v. 11, p. 1775-1795.

Gao, B.C., Heidebrecht, K.B., and Goetz, A.F.H., 1997, Atmosphere Removal Program (ATREM) Version 3.0 User's Guide: Boulder, Colo., University of Colorado, Center for the Study of Earth from Space, 27 p.

Green, R.O., Vane, G., and Conel, J.E., 1988, Determination of in-flight AVIRIS spectral, radiometric, spatial and signal-to-noise characteristics using atmospheric and surface measurements from the vicinity of the rare-earth bearing carbonatite at Mountain Pass, California, *in* Vane, G., ed., Proceedings of the Airborne Visible / Infrared Imaging Spectrometer Performance Evaluation Workshop: Pasadena, Calif., JPL Publication 88-38, Jet Propulsion Laboratory, p. 162–185.

Green, R.O., Pavri, B., Faust, J., Williams, O., and Chavoit, C., 1998, Inflight validation of AVIRIS calibration in 1996 and 1997, *in* Summaries of the Seventh JPL Airborne Earth Science Workshop: Pasadena, Calif., JPL Publication 97-21, Jet Propulsion Laboratory, p. 193–203.

Hapke, B., 1993, Theory of reflectance and emittance spectroscopy: Cambridge, Mass., Cambridge University Press, 455 p.

Hunt, G.R., Salisbury, J.W., and Lenhoff, C.J., 1973, Visible and near-infrared spectra of minerals and rocks—VII, Acidic igneous rocks: Modern Geology, v. 4, p. 217–224.

Hunt, G.R., and Ashley, R.P., 1979, Spectra of altered rocks in the visible and near-infrared: Economic Geology, v. 74, p. 1613–1629.

Klein, C., and Hurlbut, C.S., 1993, Manual of mineralogy, Twenty-first Edition: New York, John Wiley, 682 p.

Lipman, P.W., Steven, T.A., Luedke, R.G., and Burbank, W.S., 1973, Revised volcanic history of the San Juan, Uncompahgre, Silverton, and Lake City calderas in the western San Juan Mountains, Colorado: U.S. Geological Survey Journal of Research, v. 1, p. 627–642.

Lipman, P.W., Mehnert, H.H., Naeser, C.W., Luedke, R.G., and Steven, T.A., 1976, Multiple ages of mid-Tertiary mineralization and alteration in the Western San Juan Mountains, Colorado: Economic Geology, v. 71, p. 571–588.

Lucey, P.G., and Clark, R.N., 1985, Spectral properties of water ice and contaminants, *in* Klinger, J., and others, eds., Ices in the solar system: Dordrecht, Holland, D. Reidel, 954 p.

Luedke, R.G., and Burbank, W.S., 1966, Volcanism in the western San Juan mountains, Colorado: Bulletin of Volcanology, v. 29, p. 345–346.

Mast, M.A., Verplanck, P.L., Yager, D.B., Wright, W.M., and Bove, D.J., 2000, Natural sources of metals to surface waters in the Upper Animas River Watershed, Colorado, *in* ICARD 2000; Proceedings of the Fifth International Conference on Acid Rock Drainage, Volume 1: Society for Mining, Metallurgy, and Exploration, Inc., p. 513-522.

McCusker, R.T., 1982, Mount Moly progress report, 1979–1980; Drill holes 1-6: AMAX Exploration, Inc., unpublished report, 24 p.

Meyer, C., and Hemley, J.J., 1967, Wall rock alteration, *in* Barnes, H.L., ed., Geochemistry of hydrothermal ore deposits: New York, Holt, Rinehart and Winston, 670 p.

Nolin, A.W., and Dozier, J., 1993, Estimating snow grain size using AVIRIS data: Remote Sensing of Environment, v. 44, p. 231–238.

Nolin, A.W., and Dozier, J., 2000, A hyperspectral method for remotely sensing the grain size of snow: Remote Sensing of Environment, v. 74, p. 207–216.

Painter, T.H., Roberts, D.A., Dozier, J., and Green, R.O., 1998, Automated subpixel snow parameter mapping with AVIRIS data, *in* Summaries of the Seventh JPL Airborne Earth Science Workshop: Pasadena, Calif., JPL Publication 97-21, Jet Propulsion Laboratory, p. 301–307.

Porter, W.M., and Enmark, H.T., 1987, System overview of the Airborne Visible / Infrared Imaging Spectrometer (AVIRIS), *in* Vane, G., ed., Imaging spectroscopy II, Volume 834: Bellingham, Wash., International Society for Optical Engineering, p. 22–31.

Ransome, F.L., 1901, A report on the economic geology of the Silverton quadrangle, Colorado: U.S. Geological Survey Bulletin 182, 265 p.

Richards, J.A., 1994, Remote sensing digital image analysis—An introduction: Berlin, Springer-Verlag, 340 p.

Ringrose, C.R., Harmon, R.S., Jackson, S.E., and Rice, C.M., 1986, Stable isotope geochemistry of a porphyry-style hydrothermal system, West Silverton District, San Juan Mountains, Colorado, U.S.A.: Applied Geochemistry, v. 1, p. 357–373.

Rose, A.W. and Burt, D.M., 1979, Hydrothermal alteration, *in* Barnes, H.L., ed., Geochemistry of hydrothermal ore deposits, Second Edition: New York, John Wiley, 798 p.

Sabins, F.F., 1987, Remote sensing principles and interpretation: New York, Freeman and Co., 449 p.

Schemel, L.E., Kimball, B.A., and Bencala, B.A., 2000, Colloid formation and transport of aluminum and iron in the Animas River near Silverton, Colorado: Applied Geochemistry, v. 15, p. 1003–1018.

Srodon, J., and Eberl, D.D., 1984, Illite: Reviews in Mineralogy, v. 13, p. 495–544.

Steven, T.A., Hon, Ken, and Lanphere, M.A., 1995, Neogene geomorphic evolution of the central San Juan mountains near Creede, Colorado: U.S. Geological Survey Miscellaneous Investigations Series Map I–2504, scale 1:100,000.

Steven, T.A., and Lipman, P.W., 1976, Calderas of the San Juan volcanic field, southwestern Colorado: U.S. Geological Survey Professional Paper 958, 35 p.

Swayze, G.A.S., Smith, K.S., and Clark, R.N., Imaging spectroscopy—A new screening tool for mapping acidic mine waste, *in* ICARD 2000; Proceedings of the Fifth International Conference on Acid Rock Drainage, Volume 2: Society for Mining, Metallurgy, and Exploration, Inc., p. 1531–1540.

Swayze, G.A.S., Smith, K.S., Clark, R.N., Sutley, S.J., Pearson, R.M., Vance, J.S., Hageman, P.L., Briggs, P.H., Meier, A.L., Singleton, M.J., and Roth, S., 2000, Using imaging spectroscopy to map acidic mine waste: Environmental Science and Technology, v. 34, p. 47–54.

U.S. Geological Survey, 1976, Durango quadrangle topographic map: U.S. Geological Survey, scale 1:250,000.

Varnes, D.J., 1963, Geology and ore deposits of the South Silverton mining area, San Juan County, Colorado: U.S. Geological Survey Professional Paper 378–A, 56 p.

White, W.H., Bookstrom, A.A., Kamilli, R.J., Ganster, M.W., Smith, R.P., Ranta, D.E., and Steininger, R.C., 1981, Character and origin of climax-type molybdenum deposits: Economic Geology, v. 75, p. 270–316.

Wiemker, R., Rohr, K., Binder, L., Srengel, R., Stiehl, H.S., 1996, Application of elastic registration to imagery from airborne scanners, *in* Proceedings of the 18th Congress of the International Society for Photogrammetry and Remote Sensing ISPRS, Vienna, Volume 31 (B4): International Archives of Photogrammetry and Remote Sensing, p. 949–954.

Wirt, Laurie, Leib, K.J., Melick, R., and Bove, D.J., 2001, Metal loading assessment of a small mountainous sub-basin characterized by acid drainage; Prospect Gulch, upper Animas River watershed, Colorado: U.S. Geological Survey Open-File Report 01-0258, 36 p.

Yager, D.B., and Bove, D.J., 2002, Generalized geologic map of part of the upper Animas River watershed and vicinity, Silverton, Colorado: U.S. Geological Survey Miscellaneous Field Studies Map MF–2377, scale 1:48,000.

Yager, D.B., Mast, M.A., Verplanck, P.L., Bove, D.J., Wright, W.G., and Hageman, P.L., Natural versus mining-related water quality degradation to tributaries draining Mount Moly, Silverton, Colorado, *in* ICARD 2000; Proceedings of the Fifth International Conference on Acid Rock Drainage, Volume 1: Society for Mining, Metallurgy, and Exploration, Inc., p. 535–550.